Pre-eruptive magmatic processes associated with the historical (218 ± 14 aBP) explosive eruption of Tutupaca volcano (southern Peru)

Nélida Manrique, Pablo Samaniego, Etienne Médard, Federica Schiavi, Jersy Mariño, Céline C. Liorzou

Pre-eruptive magmatic processes associated with the historical (218 ± 14 aBP) explosive eruption of Tutupaca volcano (southern Peru)

Nélida Manrique[1], Pablo Samaniego[2], Etienne Médard[2], Federica Schiavi[2], Jersy Mariño[1], Céline Liorzou[3]

[1] Observatorio Vulcanológico del INGEMMET, Dirección de Geología Ambiental y Riesgo Geológico, Urb. Magisterial B-16, Umacollo, Arequipa, Peru

[2] Université Clermont Auvergne, CNRS, IRD, OPGC, Laboratoire Magmas et Volcans, F-63000 Clermont-Ferrand, France

[3] Laboratoire Géosciences Océan, Institut Universitaire Européen de la Mer, Université de Bretagne Occidentale, Rue Dumont d'Urville, 29280 Plouzané, France

Corresponding author: pablo.samaniego@ird.fr

Abstract

Magma recharge into a differentiated reservoir is one of the main triggering mechanisms for explosive eruptions. Here we describe the petrology of the eruptive products of the last explosive eruption of Tutupaca volcano (southern Peru) in order to constrain the pre-eruptive physical conditions (P-T-X_{H2O}) of the Tutupaca dacitic reservoir. We demonstrate that prior to

Pre-eruptive magmatic processes associated with the historical (218 ± 14 aBP) explosive eruption of Tutupaca volcano (southern Peru)

Nélida Manrique[1], Pablo Samaniego[2], Etienne Médard[2], Federica Schiavi[2], Jersy Mariño[1], Céline Liorzou[3]

[1] Observatorio Vulcanológico del INGEMMET, Dirección de Geología Ambiental y Riesgo Geológico, Urb. Magisterial B-16, Umacollo, Arequipa, Peru

[2] Université Clermont Auvergne, CNRS, IRD, OPGC, Laboratoire Magmas et Volcans, F-63000 Clermont-Ferrand, France

[3] Laboratoire Géosciences Océan, Institut Universitaire Européen de la Mer, Université de Bretagne Occidentale, Rue Dumont d'Urville, 29280 Plouzané, France

Corresponding author: pablo.samaniego@ird.fr

Abstract

Magma recharge into a differentiated reservoir is one of the main triggering mechanisms for explosive eruptions. Here we describe the petrology of the eruptive products of the last explosive eruption of Tutupaca volcano (southern Peru) in order to constrain the pre-eruptive physical conditions (P-T-X_{H2O}) of the Tutupaca dacitic reservoir. We demonstrate that prior to

the paroxysm, magma in the Tutupaca dacitic reservoir was low-temperature and high viscosity (735 ± 23°C), with a mineral assemblage of plagioclase, low-Al amphibole, biotite, titanite and Fe-Ti oxides, located at 8.8 ± 1.6 km depth (233 ± 43 MPa). The phenocrysts of the Tutupaca dacites show frequent disequilibrium textures such as reverse zonation, resorption zones and overgrowth rims. These disequilibrium textures suggest a heating process induced by the recharge of a hotter magma into the dacitic reservoir. As a result, high-Al amphibole and relatively high-Ca plagioclase phenocryst rims and microlites were formed and record high temperatures from just before the eruption (840 ± 45°C). Based on these data, we propose that the recent eruption of Tutupaca was triggered by the recharge of a hotter magma into a highly crystallized dacitic magma reservoir. As a result, the resident dacitic magma was reheated and remobilized by a self-mixing process. These magmatic processes induced an enhanced phase of dome growth that provoked destabilization of the NE flank, producing a debris avalanche and its accompanying pyroclastic density currents.

Keywords: Tutupaca, Peru, sector collapse, recharge, thermobarometry

Introduction

Constraining pre-eruptive magmatic processes is a key step toward understanding the triggering mechanisms of explosive eruptions. Several processes have been invoked as triggers of such events, including: (1) recharge of a differentiated reservoir by primitive magmas followed by magma mixing (e.g. Pinatubo 1991; Pallister et al. 1992), (2) self-mixing between magmas with the same composition but different temperatures and volatile contents (e.g.

43 Soufriere Hills, Montserrat 1995, Couch et al. 2001; Tungurahua 2006, Samaniego et al. 2011;
44 Ubinas 2006, Rivera et al. 2014); (3) the occurrence of large regional earthquakes (e.g. Puyehue-
45 Cordon Caulle 1960, Lara et al. 2004); and (4) the existence of a volatile-saturated magma
46 reservoir (e.g. Galeras 1990, Stix et al. 1997; Chaitén 2008, Castro and Dingwell 2009; Calbuco
47 2015, Castruccio et al. 2016).

48 Tutupaca volcano, located in the southern part of the Peruvian volcanic arc (Central
49 Volcanic Zone of the Andes) comprises a dacitic dome complex of Holocene age, which
50 experienced a large explosive eruption in historical times (218 ± 14 aBP; Samaniego et al. 2015).
51 This eruption was characterized by a sector collapse of the NE flank of the volcano, with the
52 subsequent generation of a debris avalanche and a large sequence of pyroclastic density currents
53 (Samaniego et al. 2015; Valderrama et al. 2016). The association between a debris avalanche and
54 a collapse-triggered explosive eruption has been described in the literature (*cf.* Belousov et al.
55 2007), most notably for the recent eruptions of Mt. St. Helens in 1980 (Hobblit et al. 1981),
56 Bezymianny in 1956 (Belousov 1996) and Soufrière Hills in 1997 (Voight et al. 2002). The
57 triggering mechanisms invoked for these eruptions include the presence of a pressurized magma
58 body located at very shallow levels (cryptodome) for the Mt. St. Helens and Bezymianny
59 eruptions, and a reinforced phase of dome growth for Soufrière Hills volcano.

60 In order to understand the magmatic processes and the triggering mechanism at work
61 before the last Tutupaca eruption, we use the work of Samaniego et al. (2015) and Valderrama et
62 al. (2016) as a foundation for a petrological study of the eruptive products of this eruption,
63 focusing on samples of the pyroclastic density current deposits as well as on the pre-collapse
64 domes. We also investigated some scarce magmatic enclaves found in the younger pre-collapse
65 domes. Based on these data, we constrain the pre-eruptive physical conditions of the magmas (P-

66 T-X_{H2O}), identify the petrological processes that occurred in the shallow reservoir, and propose a
67 model in which magma recharge and self-mixing in a dacitic reservoir are the triggering
68 mechanisms associated with this eruption.

69

70 **Geological setting**

71 The Tutupaca volcanic complex (TVC, 17°01'S, 70°21'W) is located in the southern part
72 of the Peruvian volcanic arc (Fig. 1a). It is part of the Central Volcanic Zone of the Andes, which
73 results from subduction of the Nazca plate beneath the South American lithosphere. The TVC is
74 constructed on top of a Mio-Pliocene plateau formed of ignimbritic and volcano-sedimentary
75 deposits (Fidel and Zavala 2001; Thouret et al. 2007; Mamani et al. 2010). It is composed of a
76 basal, lava-dominated, hydrothermally altered and glaciated edifice, as well as two younger
77 cones here called the Western and Eastern edifices, located to the north of the complex
78 (Samaniego et al. 2015). Structural development of the volcanic complex is controlled by
79 regional normal faults with a sinistral component and a roughly N140° direction that have been
80 mapped around Suches lake (Fig. 1b; Mariño et al. 2019). These structures are roughly parallel to
81 the Incapuquio fault system, which is located in a forearc setting (not shown, Benavente et al.
82 2017).

83 Eastern Tutupaca (5815 meters above sea level) is the youngest edifice of the complex
84 and is constructed on top of the hydrothermally-altered Basal Tutupaca edifice. It is composed of
85 at least seven coalescent domes of dacitic composition (64-66 wt.% SiO_2) that are not affected by
86 Pleistocene glaciations, suggesting a Holocene age (domes I to VII, Fig. 1b, 2a). The youngest
87 dome (dome VII) contains scarce mafic enclaves (only 5 small enclave samples were collected

88 during our fieldwork). The most conspicuous characteristic of this edifice is a 1 km-wide
89 horseshoe-shaped amphitheatre open to the NE. Eastern Tutupaca was affected by at least two
90 sector collapses, whose deposits were dispersed in different directions: the older deposit was
91 channelized through the Basal Tutupaca glacial valleys located to the E and SE of the volcano;
92 whereas the younger deposit crops out immediately to the NE of the amphitheatre. A large
93 explosive eruption of Tutupaca was radiocarbon dated at 218 ± 14 aBP (Samaniego et al. 2015).
94 This age is corroborated by historical accounts describing a sustained explosive activity in the
95 period between *CE* 1787 and 1802 (Zamácola y Jaúregui 1804; Valdivia 1847). This eruption
96 was characterized by a sector collapse that triggered a debris avalanche and an associated
97 explosive eruption (Fig. 1b) whose deposits spread out into the Paipatja plain to the NE of the
98 complex. On the basis of detailed field work, Samaniego et al. (2015) and Valderrama et al.
99 (2016) described the following deposits for the historical eruptions of Tutupaca: (1) a sequence
100 of pre-avalanche block-and-ash flows exposed in the Zuripujo valley to the east of the Eastern
101 Tutupaca summit (the Z-PDC deposits, Fig. 1b); (2) a debris avalanche (DA) deposit with two
102 main units of different compositions and dynamic behaviours, which is well exposed toward the
103 NE of the complex; and (3) a pyroclastic density current deposit, interlayered with the DA
104 deposit, and covering the Paipatja plain to the NE of the volcano (the P-PDC deposit, Fig. 1b,
105 2a).

106

107 Figure 1

108 Figure 2

109

Sampling and analytical methods

Based on the studies of Samaniego et al. (2015) and Valderrama et al. (2016), we focus here on the historical volcanic products of the Eastern Tutupaca edifice. Two samples with contrasting textures, including a pumiceous bomb from the P-PDC (TU-12-06A) and a dense block from a pre-avalanche dome (TU-12-42), were used for modal analyses. We used high-resolution (1200 dpi) images of thin sections scanned between two polarized sheets and Adobe Photoshop® software to do the image analysis, following the procedure described by Zhang et al. (2014). A different shade of grey was attributed to each mineral (plagioclase, amphibole, biotite, titanite, clinopyroxene, quartz, and Fe-Ti oxides), and these were distinguished from the matrix and the vesicles. We calculated the number of pixels for each mineral, as well as the total number of pixels in the image, to obtain the 2D modal percentages. Following Zhang et al. (2014) this method yields low (± 3%) discrepancies with respect to 3D estimates.

Major and trace-element whole-rock analyses (Table 1) were obtained from agate-crushed powders of 37 samples at the Laboratoire Géosciences Océan, Université de Bretagne Occidentale (Brest, France), using an Inductively Coupled Plasma-Atomic Emission Spectrometer (ICP-AES) and following the analytical procedure described by Cotten et al. (1995). Relative standard deviation (2 sigma) is ≤1% for SiO_2, ≤2% for the other major elements and ≤5% for trace elements. Major element compositions of minerals and glasses (Tables 2 to 6) were obtained at the Laboratoire Magmas et Volcans, Université Clermont Auvergne (Clermont-Ferrand, France), using a CAMECA SX-100 electron microprobe. Additional information concerning the analytical methods is included in the Supplementary material 1. Trace element compositions for selected phenocrysts (Supplementary material 2) were obtained by Laser-Ablation-ICP-MS analyses, using a 193 nm Resonetics M-50E excimer laser coupled to an

Agilent 7500cs ICP-MS. This technique uses calcium as an internal standard and measurements were calibrated relative to the NIST-612 glass. Standards NIST-612 and BCR was also measured to check the reliability of the results. The typical analytical error for most trace elements is < 10%.

Water content in melt inclusions (Table 6) was determined at the Laboratoire Magmas et Volcans using a Renishaw InVia confocal microspectrometer equipped with a 532 nm diode laser (200 mW output power), a Peltier-cooled CCD detector, a motorized XYZ stage and a Leica DM2500 M optical microscope. We used an external calibration procedure and a set of hydrous glass standards (see Schiavi et al. 2018 for details about the method). Standard glasses were analysed at the same conditions as the samples. Under these analytical conditions the precision, calculated from repeated standard measurements (relative uncertainty), is usually better than 6 %.

Petrological data

Petrography

The dome rocks, the juvenile blocks of the DA deposits and the dense blocks of the P-PDC deposits (Fig. 3a-f) are dark grey, porphyritic (~35 vol.% phenocrysts), partially vesiculated (~5 vol.%) dacites with phenocrysts of plagioclase (15-20 vol.%), amphibole (10-15 vol.%), biotite (3-5 vol.%), clinopyroxene (2-3 vol.%) and Fe-Ti oxides (1-3 vol.%), and with titanite, apatite and quartz as accessory phases (<1 vol.%). The matrix is composed of interstitial glass, with abundant microlites (<100 μm) of plagioclase, amphibole and Fe-Ti oxides. The P-PDC deposits also contain breadcrust-type bombs (Fig. 2c,d) that are light grey, vesiculated (~15

155 vol.%), have porphyritic textures (~15-20 vol.% phenocrysts) and an identical mineral
156 assemblage to the dense blocks. The scarce mafic magmatic enclaves are fine-grained and
157 rounded (2-10 cm in diameter), with a quench-textured groundmass constituted of randomly
158 oriented, interlocking, elongate or acicular crystals (Fig. 3g). The main phases are tabular
159 plagioclase (150 to 600 μm), acicular amphibole (100 to 350 μm) and biotite (100 to 250 μm)
160 and scarce Fe-Ti oxides (100-150 μm) in a mostly glassy, vesicular matrix. Also present in the
161 enclaves are some large plagioclase phenocryst with sieve textures and subhedral amphiboles (up
162 to 1-2 mm), probably derived from the host dacite. In addition, a silicic enclave (50 x 30 cm in
163 diameter) was sampled in a block from the older debris avalanche deposit of Eastern Tutupaca.
164 This enclave has a microgranular texture (Fig. 3h), and is composed of euhedral to subhedral
165 zoned plagioclase (40-45 vol.%) with amphibole inclusions, subhedral quartz (5-7 vol.%) with
166 resorption rims, amphibole (3 vol.%) with reaction rims, Fe-Ti oxides (1-2 vol.%), biotite and
167 titanite (<1 vol.%). This enclave has a glassy matrix with abundant microlites of plagioclase,
168 amphibole and Fe-Ti oxides.

169

170 Figure 3

171

172 Whole-rock major and trace elements

173 The Holocene Tutupaca eruptive products are high-K calc-alkaline dacites (Fig. 4, Table
174 1) according to the classification of Peccerillo and Taylor (1976). All samples from the Eastern
175 Tutupaca domes show very restricted dacitic compositions (64.4–66.1 wt.% SiO_2, normalized on
176 an anhydrous basis). Dense juvenile blocks included in the DA and the P-PDC deposits have

177 similar chemical characteristics (64.5– 65.9 wt.% SiO_2). In contrast, the bombs of the P-PDC
178 deposits, especially the scarce pumiceous samples (67-68 wt.% SiO_2), and the silicic enclave (68
179 wt.% SiO_2) have slightly higher silica contents. The fine-grained enclaves are of basaltic-
180 andesitic or andesitic compositions (53.0-57.9 wt.% SiO_2).

181 Comparisons between the younger (Eastern) and the older (Western and Basal Tutupaca)
182 edifices of the Tutupaca complex show that, for most major elements, Eastern Tutupaca samples
183 lie on the trend defined by the Basal and Western Tutupaca edifices (Fig. 4). This trend is
184 characterized by a progressive decrease in major elements with silica increase, except for K_2O
185 that display a positive correlation with silica. Similarly, the overall Tutupaca magmatic trend is
186 characterized by negative correlations of Sr, some transition metals (e.g. V, the Middle Rare
187 Earth Elements (MREE, e.g. Dy) and the Heavy Rare Earth Elements (HREE, e.g. Yb) with
188 silica content. In contrast, the Large Ion Lithophile Elements (LILE, e.g. Th) are positively
189 correlated with silica content (Fig. 4), whereas some scattering is observed for the Light Rare
190 Earth Elements (LREE, e.g. La, Nd), and the High Field Strength Elements (HFSE, e.g. Zr, Nb,
191 not shown). The most striking characteristic of Eastern Tutupaca eruptive products, however, is a
192 slight enrichment in LREE (e.g. La) and Sr, and a notable depletion in the MREE (e.g. Dy) and
193 HREE (e.g. Yb), which results in high La/Yb ratios (41-83) and Dy/Yb ratios (2.5-3.4) for the
194 Eastern Tutupaca samples as compared to the whole Tutupaca volcanic complex (Fig. 4*)*. Lastly,
195 the mafic enclaves represent the most primitive compositions of this volcanic complex, and
196 extend the Tutupaca magmatic trend towards low-silica concentrations.

197

198 Figure 4

199 Table 1

200

201 Mineral textures and chemistry

202 *Plagioclase* is the most abundant mineral in Tutupaca dacites (15-20 vol.%) and appears as
203 euhedral and subhedral phenocrysts and microlites. Phenocrysts have a wide range of
204 compositions from An_{24} to An_{61}, while microlites have more restricted compositions from An_{32}
205 to An_{52}. Two different groups of plagioclase phenocrysts are identified on the basis of textural
206 characteristics: (1) a dominant first group (10-15 vol.%), which includes euhedral and subhedral
207 phenocrysts with normal zoning (e.g. $An_{45\rightarrow22}$) and no evidence of disequilibrium (Fig. 3a), and
208 (2) a subordinate group (5-10 vol.%), which includes subhedral plagioclase with concentric
209 resorption zones and/or overgrowth rims 10 to 35 μm-thick with An-rich compositions (An_{42} to
210 An_{61}) and higher values of FeO* (0.4 to 0.7 wt.%, see below; Fig. 3b), phenocrysts with sieve
211 textures, and oscillatory (e.g. $An_{26\rightarrow35\rightarrow51\rightarrow30}$) or reverse (e.g. $An_{26\rightarrow55}$) zoning patterns (Fig. 5a,b;
212 Table 2).

213

214 Table 2

215

216 *Amphibole* is the second most abundant mineral phase in Tutupaca dacites (5-10 vol.%).
217 According to the classification scheme of Leake et al. (1997), amphibole phenocrysts from the P-
218 PDC, the lava domes and the enclaves include magnesio-hornblende, tschermakite, magnesio-
219 hastingsite and some scarce edenite compositions, whereas microlites from P-PDC samples are

largely magnesio-hastingsite. Amphibole phenocrysts are commonly fresh (unaltered) and euhedral, although a small subset (see below) has oxidized cores and rims, and rarely the crystals are totally replaced by an aggregate of Fe-Ti oxides, pyroxenes and plagioclase (gabbroic-type alteration, Rutherford and Hill 1993; de Angelis et al. 2013).

Three different populations have been identified. Group 1 (3-7 vol.%) includes euhedral and subhedral amphiboles (Fig. 3c, 300-1000 μm) with low-Al compositions (6-7 wt.% Al_2O_3), low Mg# of 66 to 57, with decreasing Mg# toward the rim [where Mg# = 100*Mg/(Mg + Fe^T), in mol% and Fe^T is total Fe]. The second group (2-3 vol.%) is composed of phenocrysts with thin high-Al rim overgrowths (10-20 μm; 8-11 wt.% Al_2O_3) mantling a low-Al core (Fig. 3d, 5e,f), and displaying a sharp increase in Mg# from core to rim (from 50 to 70; Fig. 5f; Table 3*)*. Included in this group are amphibole microlites with high-Al compositions, similar to those of the phenocryst overgrowth rims. The third group corresponds to amphibole from the fine-grained mafic magmatic enclaves (Fig. 3g), which have high-Al compositions and normal Mg# zoning (e.g. Mg# 68→62).

Figure 5

Table 3

Table 4

Biotite appears as euhedral and subhedral phenocrysts (3 vol.%, up to 2 mm in diameter) as well as inclusions in plagioclase and amphibole phenocrysts. Some phenocrysts display a variation in

241 FeO* (e.g. 15-19 wt.%, Table 4) and MgO (e.g. 12-17 wt.%). Some P-PDC biotites are oxidized,
242 although the degree of oxidation varies from severe to mild from one crystal to another.

243

244 *Clinopyroxene* (3 vol.%) is present as subhedral to euhedral phenocrysts (Fig. 3e, 100-300 μm),
245 as well as microlites (10-50 μm). It is also observed as a reaction product of amphibole
246 breakdown. Following the classification scheme of Morimoto et al. (1988), clinopyroxene
247 phenocrysts are augites with largely uniform $Wo_{41-44}En_{41-45}Fe_{12-16}$ compositions (Table 5) and
248 commonly show slight reverse zoning with higher Mg# rims (70→80).

249

250 *Titanite* is an accessory phase (< 1 vol.%) that appears as brown, zoned microphenocrysts and
251 phenocrysts (Fig. 3b, 200-800 μm) with euhedral, rhombic habits. Titanite phenocrysts contain
252 abundant inclusions of Fe-Ti oxides, while some titanite crystals also have reaction rims
253 composed of Fe-Ti oxides. They display reverse (e.g. 1.3→1.8 wt.% FeO*, Table 5) and
254 oscillatory (e.g. 1.3→1.8→1.4 wt.% FeO*) zoning. Titanite does not appear in the mafic
255 enclaves.

256

257 *Fe-Ti oxides* (1-2 vol.%) are present as subhedral microphenocryst and microlites (< 100 μm)
258 dispersed in the groundmass and as inclusions in some phenocrysts like plagioclase, amphibole
259 and titanite. Two types of oxides have been identified. Titanomagnetite display TiO_2
260 concentrations ranging between 3.8 and 11.4 wt.%, and ilmenite shows TiO_2 values of 34.1-50.6
261 wt.%.

262

263 Table 5

264

265 Trace elements in minerals

266 Trace element concentrations were measured in selected plagioclase, amphibole, titanite,
267 biotite (not shown) and clinopyroxene phenocrysts from P-PDC and DA samples (Fig. 6,
268 Supplementary material 2). The selected plagioclases correspond to the previously defined first
269 group and exhibit a LREE enriched spectrum with a positive Eu anomaly and low concentrations
270 of MREE and HREE. The compositional spectra for clinopyroxene are uniform and concave,
271 showing high concentrations of MREE compared to LREE and HREE, and no Eu anomaly.
272 Concerning amphibole, the high-Al phenocrysts display very homogeneous, REE fractionated,
273 concave spectra with a small negative Eu anomaly, whereas the low-Al amphiboles display a
274 wide REE variability, with LREE-enriched, HREE-depleted spectra and a strong negative Eu
275 anomaly. Lastly, titanite analyses exhibit REE-fractionated spectra, characterized by extremely
276 high values of all REE, and a slight negative Eu anomaly. In addition, for the plagioclase and
277 amphibole phenocrysts, the core compositions display lower REE values than those of the rims
278 (Fig. 6). It should be noted that the low-Al amphibole, and to a lesser extent high-Al amphibole
279 and titanite, exhibit Eu negative anomalies, which indicates the contemporaneous crystallization
280 of plagioclase, amphibole and titanite.

281

282 Figure 6

283

284 Chemical composition of interstitial glass and melt inclusions

285 Interstitial matrix glasses (MG) (Table 6) from recent dacitic samples display rhyolitic
286 compositions (70-78 wt.% SiO_2, Fig. 7) with an average value of 74.4 ± 2.3 wt.% SiO_2 (n=21, n
287 being the number of analyses) for P-PDC, and 73.8 ± 2.8 wt.% SiO_2 (n=2) for recent domes and
288 debris avalanche blocks. When plotted on Harker diagrams, MG compositions show a wide
289 scattering for some major elements (K_2O, Al_2O_3, CaO; Fig. 7) but they form an extension to the
290 whole-rock data toward silica-rich compositions. These glass compositions are enriched in K_2O
291 (3.3-6.4 wt.%, Fig. 7) compared to whole-rocks, and they show low concentrations of Al_2O_3
292 (9.9-17.1 wt.%), FeO* (0.7-1.6 wt.%), CaO (0.2-3.4 wt.%), and MgO (0.0-0.7 wt.%). These
293 features suggest that scattering probably results from the presence of tiny (a few μm) plagioclase
294 microlites on the analysed spot. Plagioclase- and amphibole-hosted melt inclusions (MI) display
295 much more uniform values (74-78 wt.% SiO_2), and they also plot at the high-silica end of the
296 whole-rock magmatic trend. Water contents measured by Raman spectroscopy in plagioclase-
297 hosted MI range between 1.5 and 2.5 (2.1 ± 0.3; n=11) wt.%, whereas amphibole-hosted MI
298 display slightly higher values, ranging from 1.5 to 3.7 (2.5 ± 0.8; n=9) wt.% H_2O.

299

300 Figure 7

301 Table 6

302

303 **Pre-eruptive P–T–X_{H2O} conditions**

Experimental constraints

Pre-eruptive physical conditions (P–T–X_{H2O}) can be constrained by comparison of the mineral assemblage observed in Tutupaca dacites with experimental studies on analogous magma compositions. The dacitic magmas of Mt. St. Helens (Rutherford and Devine 1988), Pinatubo (Prouteau and Scaillet 2003) and Unzen (Holtz et al. 2005) have a similar major element composition to those of Tutupaca. Amphibole crystallization in these dacitic magmas places strong constraints in terms of P-T-X_{H2O}. Amphibole is stable at <900°C, 160-300 MPa, and a water content of between 4-6 wt.% (Scaillet and Evans 1999; Prouteau and Scaillet 2003; Holtz et al. 2005). Biotite is stable at lower temperatures (775-800°C) and pressures (100–200 MPa), while the water content can range between 5 and 7 wt.% (Holtz et al. 2005; Castro and Dingwell 2009). The presence of titanite in dacitic magmas also provides additional constraints about the crystallization conditions. Experimental work on the Fish Canyon Tuff dacite (Hayden et al. 2008) shows that titanite crystallized at 745-780°C, and a pressure of between 100-300 MPa. Based on these experimental data, we suggest that Tutupaca dacitic magmas should have equilibrated at 750–800°C, 100–300 MPa and should contain at least 4–6 wt.% water. We should stress that these are first-order estimates. Taking advantage of the ubiquitous presence of amphibole on Tutupaca samples, we applied several amphibole-based thermobarometers in order to better constrain the P-T-X_{H2O} conditions of Tutupaca dacites.

Amphibole stoichiometry

Amphibole compositions in calc-alkaline rocks are controlled by different substitutions that are function of pressure, temperature, and melt composition (Poli and Schmidt 1992;

326 Bachmann and Dungan 2002; de Angelis et al. 2013). The main exchange mechanisms are: (1)
327 the Tschermack substitution [$Si_{(Tsite)} + Mg_{(Csite)} = {}^{IV}Al_{(Tsite)} + {}^{VI}Al_{(Csite)}$]; (2) the Ti-Tschermack
328 substitution [$2\ Si_{(Tsite)} + Mg_{(Csite)} = 2\ {}^{IV}Al_{(Tsite)} + Ti_{(Csite)}$]; and (3) the edenite substitution [$Si_{(Tsite)}$
329 $+ \square_{(Asite)} = {}^{IV}Al_{(Tsite)} + (Na+K)_{(Asite)}$]. The Tschermack substitution is correlated with
330 crystallization pressure, whereas the Ti-Tschermack and edenite substitutions are mostly
331 sensitive to temperature variations (Blundy and Holland 1990; Poli and Schmidt 1992; Holland
332 and Blundy 1994).

333 Tutupaca amphiboles plot in two different groups defined by their ^{IV}Al, Si and Na+K
334 contents, whereas ^{VI}Al and Mg# are almost constant (Fig. 8). The difference between the two
335 groups corresponds to an edenite substitution, implying a strong difference in temperature, but
336 little variations in pressure. For the recent dacitic rocks (RD and P-PDC), the phenocrysts show
337 both low and high ^{IV}Al (0.8 – 1.3 and 1.5 – 2.0 atoms per formula unit –a.p.f.u.), whereas
338 microlites show only high ^{IV}Al content (1.7 – 2.0) (i.e. high temperature). Amphiboles from the
339 fine-grained mafic enclaves also have high ^{IV}Al values (1.5 – 2.1 a.p.f.u.), and show a weak
340 increase in ^{VI}Al (up to 0.4 a.p.f.u.).

341

342 Figure 8

343

344 Temperature

345 The paragenesis of Tutupaca dacites is suitable for temperature estimates using
346 amphibole-plagioclase geothermometry (Blundy and Holland 1990). The edenite-richterite and
347 edenite-tremolite formulations of Holland and Blundy (1994) apply to silica undersaturated

348 (quartz-free) and silica saturated assemblages, respectively. Although the Tutupaca dacites (and
349 the silicic enclave) do contain scarce anhedral to subhedral quartz crystals (Fig. 3f), their
350 rounded shapes and corrosion gulfs suggest these crystals might not be at equilibrium with the
351 rest of the paragenesis. We thus applied the quartz-free edenite-richterite formulation to
352 amphibole-plagioclase pairs that demonstrate textural evidence of equilibrium, including
353 touching euhedral crystals, or inclusions of amphibole in plagioclase phenocrysts. In addition,
354 because this thermometer is not very sensitive to pressure changes, we fixed the equilibrium
355 pressure to 250 MPa (see below). Different temperature estimates were obtained from low-Al
356 amphiboles (phenocryst cores) and high-Al amphiboles (overgrowth rims of phenocrysts and
357 microlites). Low-Al amphibole-plagioclase pairs yield temperatures in the range of 703 to 797°C
358 (mean value of 735 ± 23°C, n=20), whereas rather higher temperatures of 789 to 921°C (835 ±
359 41°C, n=20) were obtained for high-Al amphibole-plagioclase pairs. In addition, amphibole-
360 plagioclase pairs from the mafic enclaves also yield high temperatures (791-921ºC, 840 ± 45ºC,
361 n=11), consistent with values obtained from high-Al amphibole rims and microlites. Variations
362 in ^{IV}Al *vs.* temperature (T) in both amphibole groups (Fig. 9a) show similar relationships
363 between the calculated T and the Mg# (Fig. 9b), with the higher temperatures corresponding to
364 those amphiboles that have both higher Al content and Mg#. This behaviour has been previously
365 described for amphibole phenocrysts from Soufrière Hills volcano by Rutherford and Devine
366 (2003).

367 Temperatures estimated using amphibole and plagioclase were corroborated with the Zr-
368 in-titanite thermometer (Hayden et al. 2008), which was calibrated for magmatic titanite in
369 equilibrium with zircon, quartz and rutile. The Zr content in titanite is strongly dependent on the
370 temperature and magma composition. We consider that the interstitial melt in Tutupaca dacitic

371 magma is close to SiO_2 and TiO_2 saturation (70-78 wt.% SiO_2 and up to 0.52 wt.% TiO_2), and
372 thus its TiO_2 and SiO_2 activities are almost 1. Zr concentrations of titanite measured by LA-ICP-
373 MS for two phenocrysts range from 488 to 588 ppm and yield temperatures around 747 ± 4°C
374 (n=4). This is similar to the temperatures calculated for the low-Al amphiboles (735 ± 23°C).

375

376 Figure 9

377

378 In summary, amphiboles that record the highest temperatures display high-Al
379 compositions and correspond to the overgrowth rims of phenocrysts or the microlites in dome
380 rocks and the P-PDC products, as well as the amphiboles from the fine-grained mafic enclaves.
381 In contrast, phenocrysts with low-Al compositions show globally lower temperatures, and
382 correspond to the phenocryst cores from the lava domes and the P-PDC, as well as amphiboles in
383 the silicic enclave. Thus, the aluminium reverse zoning patterns described in amphiboles from
384 the second group (Fig. 5e,f) indicate an increase in temperature. These results confirm the
385 existence of two different parageneses in Tutupaca magmas: (1) a dominant low-temperature
386 paragenesis (735 ± 23°C), represented by the phenocryst cores of the dacites and the silicic
387 enclave (low-Al amphibole + plagioclase + biotite + titanite + Fe-Ti oxides ± quartz); and (2) a
388 high-temperature paragenesis (840 ± 45°C), represented by phenocryst rims of the dacites and
389 the mafic enclaves (high-Al amphibole + plagioclase + Fe-Ti oxides ± clinopyroxene).

390

391 Pressure

392 The Al-in-hornblende geobarometer has been calibrated experimentally by several
393 authors (i.e., Johnson and Rutherford 1989; Schmidt 1992; Mutch et al. 2016) and is widely used
394 to estimate the crystallization pressure of calc-alkaline magmas. This formulation postulates that
395 the Al content (Al_{total}) of amphibole is controlled by total pressure when buffered by a mineral
396 assemblage composed of plagioclase, biotite, quartz, sanidine, titanite and Fe-Ti oxides. Al_{total},
397 however, is also sensitive to changes in temperature (edenite and Ti-Tschermack substitutions)
398 (Poli et Schmidt 1992; Anderson et Smith 1995; Bachmann et Dungan 2002), therefore Al-in-
399 hornblende barometers can only be used within the specific temperature range at which they
400 have been calibrated. Recently, Ridolfi et al. (2010) and Ridolfi and Renzulli (2012) proposed
401 new calibrations to estimate temperature, pressure, fO_2, melt H_2O, and melt major oxide
402 compositions from amphiboles crystallized over a large compositional range (from basalts to
403 dacites). This model, however, does not take into account the influence of temperature on Al_{total},
404 and its validity has been challenged (e.g., Erdmann et al. 2015, Kiss et al. 2014; Shane and Smith
405 2013). Improved calibrations either take into account the influence of temperature on Al_{total}
406 (Anderson and Smith 1995), or separate the influence of temperature and pressure by using only
407 ^{VI}Al for geobarometry (Médard and Le Pennec 2019, submitted).

408 The low-temperature (735 ± 23°C) paragenesis observed in the phenocryst cores of the
409 Tutupaca dacites and in the silicic enclave fit the requirements for use of the traditional Al-in-
410 hornblende calibrations. Using 127 amphibole analyses from the P-PDC deposit and the
411 youngest domes gives pressure estimates of 246 ± 27 MPa with the best-suited barometer (Mutch
412 et al. 2016, calibrated at ~733°C). The calibrations of Anderson and Smith (1995) and Médard
413 and Le Pennec (2019) give identical results and are all consistent within errors (Table 7).

414 Pressure estimates for the silicic enclave are within error of those for the Tutupaca dacites (Table
415 7).

416 Pressure estimates for the high-temperature (840 ± 45°C) phase assemblage are more
417 difficult to compute, because the equilibrium paragenesis used for Al-in-hornblende
418 geobarometry is not present. Based on 72 high-Al amphibole compositions from the Paipatja
419 pyroclastic density currents and the youngest domes, the temperature-corrected calibration of
420 Anderson and Smith (1995) and the temperature-independent calibration of Médard and Le
421 Pennec (2019) give pressure estimates within error of those for the low-temperature mineral
422 assemblage. The calibration of Ridolfi and Renzulli (2012) specifically excluded low-
423 temperature data (< 800°C), so it cannot be used for the low-temperature amphiboles. Although it
424 should be used with caution due to temperature effects on Al-in-amphibole barometer, results for
425 high-temperature amphiboles are in agreement with other barometers (Table 7).

426 In the absence of a better barometer for the mafic enclaves (neither the calibration of
427 Anderson and Smith (1995) nor those of Médard and Le Pennec (2019) have been calibrated for
428 andesitic compositions), the calibration of Ridolfi and Renzulli (2012) gives pressure estimates
429 of 254 ± 59 MPa, within error of estimates made from the low-temperature paragenesis. All
430 these measurements are consistent with a single depth of magma storage below Tutupaca
431 volcano prior to the latest eruption. The most accurate determinations are those made on the low-
432 Al amphiboles, because of the better-constrained calibration for low-temperature, low-variance
433 mineral assemblages. The average pressure from all three calibrations used on low-Al
434 amphiboles is 233 ± 43 MPa. Assuming lithostatic conditions and considering an upper crust
435 bulk density of 2700 kg/m^3 (Kono et al. 1989), the depth of the magma storage region under
436 Tutupaca is calculated between 7 and 11 km (8.8 ± 1.6 km).

437

438 Table 7

439

440 Water content

441 Lange et al. (2009) proposed a hygrometer based on the plagioclase-melt exchange
442 reaction between the anorthite and albite components. More recently, Waters and Lange (2015)
443 recalibrated this hygrometer for a temperature range of 750 to 1244 °C, and pressures of up to
444 350 MPa with a standard error of 0.35 wt.% H_2O. Using our temperature estimates obtained from
445 the amphibole-plagioclase thermometer we applied this formulation to 18 matrix glass -
446 plagioclase rim pairs from Tutupaca dacites (RD, DA and P-PDC), which yielded water contents
447 between 3.7 to 6.4 wt.%. Applying the same method to 11 melt inclusions in plagioclase
448 phenocrysts from P-PDC (sample TU-12-77C) yielded similar results (3.5-4 wt.% H_2O). Water
449 contents measured by Raman spectroscopy in selected plagioclase-hosted melt inclusions are
450 noticeably lower than those estimated by the Waters and Lange (2013) hygrometer. We suggest
451 these relatively low water contents can be explained by post-entrapment water loss due to rapid
452 diffusion and re-equilibration into the gas bubble or the host crystal during magma ascent (Chen
453 et al. 2011; Gaetani et al. 2012; Lloyd et al. 2012). For this reason, the measured water content in
454 MI are considered minimum values. In summary, we conclude that the pre-eruptive water
455 content for Tutupaca dacite was at least 4 and probably 6 wt.%, in good agreement with
456 experimental phase equilibrium for dacitic systems.

457

458 **Pre-eruptive magmatic processes**

459 Origin of the dacitic magma reservoir

460 Based on the geochemical and mineralogical characteristics of Tutupaca eruptive
461 products, we can reconstruct the magmatic processes that produced the dacitic magmas. The
462 decrease in CaO, Al_2O_3 (Fig. 4) and Na_2O contents with increasing SiO_2 suggest progressive
463 crystallization of plagioclase, whereas the decrease in TiO_2, Fe_2O_3* and P_2O_5 with differentiation
464 suggests fractionation of titanite, titanomagnetite, and apatite. Trace element systematics also
465 provide some key constraints on the differentiation process. A decrease in Sr, Eu and Yb suggest
466 a significant role of plagioclase and amphibole crystallization, while the negative trends for Ni,
467 Sc, V are attributed to fractionation of clinopyroxene. Thus, the dacitic Tutupaca magma was
468 generated by a fractional crystallization process involving plagioclase, amphibole and biotite
469 with minor amounts of clinopyroxene, titanite, apatite and Fe-Ti oxides. Although a more
470 detailed investigation of the evolution of the Tutupaca magmas would be interesting, it is beyond
471 the scope of this paper. We do note, however, some striking differences between the older Basal
472 and Western Tutupaca and the younger Eastern Tutupaca dacites (Fig. 4). The recent Eastern
473 Tutupaca samples display high La/Yb and Dy/Yb ratios that cannot be explained by an upper
474 crustal fractional crystallization process. The only mineral able to produce such a REE
475 fractionation is garnet, which is stable only at very high pressures, probably at the base of the
476 Andean arc crust (*cf.* Mamani et al. 2010). In addition to this fractional crystallization sequence,
477 crustal assimilation took place during ascent of the magmas through the thick Central Andean
478 crust of the Peruvian arc (*cf.* Mamani et al. 2010; Samaniego et al. 2016; Rivera et al. 2017).

479

480 Recharge processes into the dacitic magma chamber

481 Tutupaca samples are characterized by the occurrence of frequent and conspicuous
482 disequilibrium textures suggesting that recharge and mixing processes occurred prior to eruption.
483 The main characteristics we observed in Tutupaca dacites are:

484 - Reverse ($An_{27\rightarrow61}$) and oscillatory ($An_{32\rightarrow44\rightarrow31\rightarrow55}$) zoning patterns in plagioclase
485 phenocrysts (second group), which display frequent dissolution surfaces and 10-35 μm
486 overgrowth rims. These rims are enriched in CaO ($An_{42\text{-}61}$) and show relatively high
487 FeO* contents (0.4-0.6 wt.%). Some plagioclase phenocrysts also display sieve or spongy
488 textures as concentric alteration zones or rims.

489 - Reverse zoning and overgrowth rims on amphibole phenocrysts (described as the second
490 group). These rims are enriched in Al (8-11 wt.% Al_2O_3) relative to the cores (6-7 wt.%
491 Al_2O_3), and display high MgO concentrations (Mg# 50-70). Amphibole microlites also
492 have high-Al and -Mg contents, indicating that they grew at higher temperature and from
493 a more mafic melt. Some amphiboles show reaction rims composed of Fe-Ti oxides,
494 pyroxene and plagioclase (e.g. gabbroic-type alteration, de Angelis et al. 2013).

495 - Clinopyroxene phenocrysts also show slight reverse zoning with a core-to-rim increase in
496 MgO and CaO.

497 - Titanite phenocrysts display reverse and oscillatory zoning, with an increase in FeO*
498 from core to rim. Some phenocrysts show reaction rims formed mainly by Fe-Ti oxides.

499 - Quartz xenocrysts (or antecrysts) in dacites are anhedral with rounded rims and
500 embayments that suggest they suffered resorption process.

501 - Presence of scarce mafic enclaves, which is indicative of magma mingling.

Such disequilibrium features in arc magmatic systems are generally explained as having resulted from two different processes (Couch et al. 2001; Ruprecht and Wörner 2007): (1) physical or compositional mixing between two magmas of different composition and physical properties; and (2) thermal or self-mixing, which means that a hot and/or mafic magma is intruded into the base of a more silicic magma chamber, resulting in heating-induced convection of the magma reservoir without physical mixing between the mafic magma and the pre-existing silica-rich magma.

In order to discriminate between these mechanisms, some researchers use the systematic variations in An and FeO* (and to a lesser extent MgO) contents in plagioclase (Hattori and Sato 1996; Ruprecht and Wörner 2007; Humphreys et al. 2009; Ruprecht et al. 2012). The Fe partitioning in plagioclase varies as a function of the An content, as well as of temperature, degree of oxidation and water content of the co-existing magma (Bindeman et al. 1998; Ginibre et al. 2002). However, the predicted effects of these parameters on plagioclase FeO* content are null or relatively small (Ruprecht and Wörner 2007; Humphreys et al. 2009; Hattori and Sato 1996). Thus, an increase of FeO* correlated with An contents reflects a change in the host magma composition. This change can be a consequence of physical mixing between a differentiated and a mafic magma. On the contrary, a mostly flat trend, characterized by a change in the An content without a FeO* increase, mostly reflects a thermal or self-mixing process. We should stress that these are non-exclusive processes, because the heat source for self-mixing is often associated with a recharge event (Couch et al. 2001). In addition, heating may dissolve mafic phenocrysts and change the composition of the interstitial melt, thus potentially resulting in changes in plagioclase compositions. As we see in the following paragraph, magmatic systems

524 display intermediate situations in which both physical (compositional) and thermal (self-) mixing
525 occur.

526 In Tutupaca dacites we observe a rough positive trend between An and FeO* in plagioclase
527 with a quite limited chemical variation (An_{25-60} and 0.1-0.6 wt.% FeO*, Fig. 10). This pattern
528 differs from those observed at others well-studied magmatic systems such as Pinatubo (Hattori
529 and Sato 1996), Quizapu (Ruprecht et al. 2012), Misti-Andahua (Ruprecht and Wörner 2007;
530 Tepley et al. 2013), Soufrière Hills (Humphreys et al. 2009) or Tungurahua (Samaniego et al.
531 2011). For example, plagioclase compositions for the Misti-Andahua and Soufriere Hills
532 volcanic systems show a larger chemical variation (An_{25-90} and 0.1-1.2 wt.% FeO*) and a
533 complex behaviour, with a rough An-FeO* positive correlation below An_{60} and a double trend
534 above An_{60} (increase in An at almost constant FeO*, and high FeO* at almost constant An, Fig.
535 10). We thus suggest that Tutupaca plagioclases record a limited physical mixing process
536 compared to other systems, whereas self-mixing is the dominant process, as evidenced by the
537 scarcity of mafic enclaves.

538

539 Figure 10

540

541 Time constraints

542 Geochronological data reported by Samaniego et al. (2015) show identical ages for the
543 pre-avalanche (i.e. Z-PDC) and the syn-avalanche pyroclastic events (i.e. P-PDC). This suggests
544 that the time between these two eruptions is too small to be resolved by radiocarbon dating,
545 arguing for a time frame of some years to a few decades. In order to confirm this hypothesis, we

546 investigated the sharp core-to-rim transitions observed in plagioclase and amphibole phenocrysts
547 (Figures 5b,f). These transitions indicate that little diffusion happened between the crystallisation
548 of the rim and the eruption. To better constrain this timing, we modelled Mg diffusion at the
549 interface between the core and the rim of a selected crystal, whose major elements composition
550 and core-rim transition is representative of the group 2 plagioclases. A simple model of diffusion
551 in an infinite slab, starting with a step function (Lasaga 1998), diffusion coefficients from Van
552 Orman et al. (2014), an average An content of 60 %, and a temperature of 835 °C, produced
553 modelled diffusion times of 1 year (corresponding figure in Supplementary material 3), with
554 acceptable values between a few months and 10 years. The same calculation done for K, using
555 the diffusion coefficients of Giletti and Shanahan (1997) also requires diffusion times shorter
556 than 10 years, with a best fit for a diffusion time of 1 year. We propose that after injection of new
557 magma into the base of the reservoir, the resident magma gets heated by about 100 °C, and then
558 starts cooling and recrystallizing. The modelled timescales represent the time between the
559 beginning of the recrystallization of the magma and its emplacement at the surface, and thus
560 provide a maximum value for the duration of the eruptive phase. Although there are large
561 uncertainties on the measurements and models, these data would indicate that the entire eruptive
562 phase lasted at most 10-20 years, and more likely a few years.

563

564 Triggering mechanism of the eruption

565 The recharge of a hot magma in a differentiated reservoir is a recurrent process in many
566 volcanoes around the world, such as Soufriere Hills (Murphy et al. 2000; Couch et al. 2001;
567 Rutherford and Devine 2003), Unzen (Holtz et al. 2005), Quizapu (Ruprecht and Bachmann
568 2010), Tungurahua (Samaniego et al. 2011, Andujar et al. 2017) and Ubinas (Rivera et al. 2014).

569 This process produces re-heating of the "resident" magma, generating volatile exsolution and a
570 subsequent pressurization of the magma reservoir (Murphy et al. 2000; Rubin et al. 2017). In
571 addition, hot magma recharge decreases the viscosity of a differentiated magma, enabling
572 remobilization and convection in the reservoir, and triggering explosive (i.e. Soufriere Hills,
573 Murphy et al 2000; Couch et al. 2001) or effusive eruptions (i.e. Quizapu, Ruprecht and
574 Bachmann 2010). At Tutupaca volcano, the dacitic reservoir is located at 7-11 km depth (233 ±
575 43 MPa), at an initial temperature of 735 ± 23°C, with a water content of at least 4-6 wt.%. The
576 presence of reverse zoning and overgrowth rims in plagioclase and amphibole suggests that these
577 disequilibrium textures were produced by an increase in temperature of the magmatic system.
578 This change in temperature was due to intrusion of a hotter magma (Fig. 11) that is represented
579 by the scarce fine-grained mafic enclaves, which yield the highest estimated temperatures (840 ±
580 45°C). Following the magma intrusion at the base of the dacitic reservoir, magma viscosity
581 decreased and strong convection began, enhancing magma ascent and degassing, which could
582 explain the lower water content measured in melt inclusions (< 4 wt.%). Due to the viscosity
583 decrease and degassing, the highly crystallized dacitic magma became susceptible to eruption,
584 magma ascent increased and as a result an enhanced dome-forming eruption begun, which was
585 responsible for the development of the pre-avalanche dome complex. The rapid dome growth,
586 confirmed by the short timescale (some years up to a few decades) between magmatic recharge
587 and eruption, resulted in gravitational instability that subsequently triggered sector collapse of
588 Tutupaca's North-East flank (Samaniego et al. 2015; Valderrama et al. 2016), generating a debris
589 avalanche and its accompanying pyroclastic density currents.

590

591 Figure 11

592

593 **Conclusions**

594 The erupted products of the Tutupaca historical eruption are chemically homogeneous
595 (63.2-68.0 wt.% SiO_2), porphyritic (20-35 vol.%) dacites with a mineral assemblage composed
596 of plagioclase, hornblende, biotite, clinopyroxene and Fe-Ti oxides together with some accessory
597 minerals such as titanite, apatite and quartz. The phenocrysts from the Tutupaca dacites show
598 common disequilibrium textures such as reverse zonation, resorption zones and overgrowth rims.
599 These disequilibrium textures suggest a heating process triggered by the intrusion of a hot
600 magma into a dacitic magma reservoir. Based on thermobarometric analysis, the initial
601 temperature of the dacitic reservoir is estimated to be between 703 and 797°C (with an average
602 of 735 ± 23°C) at a pressure of 230 ± 58 MPa, corresponding to a depth range between 7 and 11
603 km, and a water content between 4 and 6 wt.%. The few fine-grained mafic enclaves (53-57
604 wt.% SiO_2), which are present in the younger dacite domes, give a higher range of temperature
605 between 789 and 921°C (840 ± 45°C). Based on these data, we propose that the recent eruption
606 of Tutupaca was triggered by the recharge of a hotter magma into a highly crystallized dacitic
607 magma reservoir. As a result, the resident dacitic magma was reheated and remobilized by a self-
608 mixing process that include little, if any, physical mixing with the mafic magma. These
609 magmatic processes induced an enhanced dome-growth phase that destabilized the NE flank of
610 the volcano and produced the debris avalanche and its accompanying pyroclastic density
611 currents.

612

613 **Acknowledgements**

This work is part of a Peruvian–French cooperation programme carried out between the Instituto Geológico, Minero y Metalúrgico (INGEMMET, Peru) and the Institut de Recherche pour le Développement (IRD, France). We warmly thank F. van Wyk de Vries for improvements to the English in the manuscript. We are grateful to P. Ruprecht and an anonymous reviewer for their constructive comments and J. Fierstein for the editorial handling. This is Laboratory of Excellence ClerVolc contribution n° XX.

References

Anderson JL, Smith DR (1995) The effects of temperature and fO_2 on the Al-in-hornblende barometer. Am Mineral 80:549 – 559

Andujar J, Martel C, Pichavant M, Samaniego P, Scaillet B, Molina I (2017) Structure of the plumbing system at Tungurahua volcano, Ecuador: Insights from phase equilibrium experiments on July-August 2006 eruption products. J Petrol 58:1249-1278

Bachmann O, Dungan MA (2002) Temperature-induced Al-zoning in horblendes of the Fish Canyon magma, Colorado. Am Mineral 87:723 – 738

Belousov A (1996) Deposits of the 30 March 1956 directed blast at Bezymianny volcano. Bull Volcanol 57:649–662

Belousov A, Voight B, Belousova M (2007) Directed blasts and blast-generated pyroclastic density currents : a comparison of the Bezymianny 1956, Mount St Helens 1980, and Soufrière Hills, Montserrat 1997 eruptions and deposits. Bull Volcanol 69:701–740

634 Benavente C, Zerathe S, Audin L, Hall SR, Robert X, Delgado F, Carcaillet J, ASTER Team
635 (2017) Active transpressional tectonics in the Andean forearc of southern Peru quantified
636 by ^{10}Be surface exposure dating of an active fault scarp. Tectonics 36,
637 doi:10.1002/2017TC004523.

638 Bindeman IN, Davis AM, Drake MJ (1998) Ion microprobe study of plagioclase- basalt partition
639 experiments at natural concentration levels of trace elements. Geochim. Cosmochim. Acta
640 62:1175–1193

641 Blundy J, Holland T (1990) Calcic amphibole equilibria and a new amphibole-plagioclase
642 geothermometer. Contrib Mineral Petrol 104:208-224

643 Castro JM, Dingwell DB (2009) Rapid ascent of rhyolitic magma at Chaitén volcano, Chile,
644 Nature 461:780-783

645 Castruccio A, Clavero J, Segura A, Samaniego P, Roche O, Le Pennec JL, Droguett B (2016)
646 Eruptive parameters and dynamics of the April 2015 sub-Plinian eruptions of Calbuco
647 volcano (southern Chile). Bull Volcanol 78:62

648 Chen Y, Provost A, Schiano P, Cluzel N (2011) The rate of water loss from olivine-hosted melt
649 inclusions. Contrib Mineral Petrol 162: 625–636

650 Cotten J, Le Dez A, Bau M, Caroff M, Maury RC, Dulski P, Fourcade S, Bohn M, Brousse R
651 (1995) Origin of anomalous rare-earth element and Yttrium enrichments in subaerial
652 exposed basalts: evidence from French Polynesia. Chem Geol 119:115–138

653 Couch S, Sparks RSJ, Carroll MR (2001) Mineral disequilibrium in lavas explained by
654 convective self-mixing in open magma chambers. Nature 41:1037-1039

655 De Angelis SH, Larsen J, Coombs M (2013) Pre-eruptive magmatic conditions at Augustine
656 volcano, Alaska, 2006: Evidence from amphibole geochemistry and textures. J Petrol
657 54:1939-1961

658 Erdmann S, Martel C, Pichavant M, Kushnir A (2014) Amphibole as an archivist of magmatic
659 crystallization conditions: problems, potential, and implications for inferring magma storage
660 prior to the paroxysmal 2010 eruption of Mount Merapi, Indonesia. Contrib Mineral Petrol
661 167:1016

662 Fidel L, Zavala B (2001) Mapa preliminar de amenaza volcánica del volcán Tutupaca. Boletín
663 24, Serie C: Geodinámica e Ingeniería Geológica, INGEMMET, 109 p

664 Gaetani GA, O'Leary JA, Shimizu N, Bucholv CE, Newville M (2012) Rapid re-equilibration of
665 H_2O and oxygen fugacity in olivine-hosted inclusions. Geology 40:915-918

666 Giletti BJ, Shanahan TM (1997) Alkali diffusion in plagioclase feldspar. Chemical Geology
667 139:3–20

668 Ginibre C, Wörner G, Kronz A (2002) Minor- and trace-element zoning in plagioclase:
669 implications for magma chamber processes at Parinacota Volcano, northern Chile.
670 Contributions to Mineralogy and Petrology 143:300-315

671 Hattori K, Sato H. (1996) Magma evolution recorded in plagioclase zoning in 1991 Pinatubo
672 eruption products. American Mineralogist 81: 982-994

673 Hayden LA, Watson EB, Wark DA (2008) A thermobarometer for sphene (titanite). Contrib
674 Mineral Petrol 155:529–540

675 Hoblitt RP, Miller CD, Vallance JW (1981) Origin and stratigraphy of the deposit produced by

676 the May 18 directed blast. In: Lipman PW, Mullineaux DR (eds) The 1980 eruptions of
677 Mount St. Helens, Washington. USGS Prof Paper 1250:401–419

678 Holland T, Blundy J (1994) Non-ideal interactions in calcic amphiboles and their bearing on
679 amphibole-plagioclase thermometry. Contrib Mineral Petrol 116:433–447

680 Holtz F, Sato H, Lewis J, Behrens H, Nakada S (2005) Experimental Petrology of the 1991 –
681 1995 Unzen Dacite , Japan . Part I : Phase Relations , Phase Composition and Pre-eruptive
682 Conditions. J Petrol 46:319–337

683 Humphreys MCS, Christopher T, Hards V (2009) Microlite transfer by disaggregation of mafic
684 inclusions following magma mixing at Soufrière Hills volcano Montserrat. Contrib.
685 Mineral. Petrol. 157:609–624. doi:10.1007/s00410-008-0356-3

686 Johnson MC, Rutherford MJ (1989) Experimental calibration of the aluminum-in-hornblende
687 geobarometer with application to Long Valley caldera (California) volcanic rocks. Geology
688 17:837-841

689 Kiss B, Harangi S, Ntaflos T, Mason PRD, Pál-Molnár E (2014) Amphibole perspective to
690 unravel pre-eruptive processes and conditions in volcanic plumbing systems beneath
691 intermediate arc volcanoes: a case study from Ciomadul volcano (SE Carpathians). Contrib
692 Mineral Petrol 167:986

693 Kono M, Fukao Y, Yamamoto A (1989) Mountain building in the Central Andes. J Geophys Res
694 94:3891–3905

695 Lange R, Frey H, Hector J (2009) A thermodynamic model for the plagioclase-liquid
696 hygrometer/thermometer. Am Mineral 94:494-506

697 Lara LE, Naranjo JA, Moreno H (2004) Rhyodacitic fissure eruption in Southern Andes (Cordón
698 Caulle; 40.5°S) after the 1960 (Mw:9.5) Chilean earthquake: a structural interpretation. J
699 Volcanol Geotherm Res 138:127–138

700 Lasaga AC (1998). Kinetic theory in the earth sciences. Princetown series in geochemistry.
701 Princeton University Press, Princeton, N.J.

702 Leake BE, Woolley AR, Arps CES, Birch WD, Gilbert MC, Grice JD, Hawthorne FC, Kato A,
703 Kisch HJ, Krivovichev VG, Linthout K, Laird J, Mandarino JA, Maresch WV, Nickel EH,
704 Rock NMS, Schumacher JC, Smith DC, Stephenson CN, Ungaretti L, Whittaker EJW,
705 Youzhi G (1997) Nomenclature of amphiboles: report of the Subcommittee on Amphiboles
706 of the International Mineralogical Association, commission on new minerals and minerals'
707 names. Am Mineral 82:1019–1037

708 Lloyd AS, Plank T, Ruprecht P, Hauri EH, Rose W (2012) Volatile loss from melt inclusions in
709 pyroclasts of differing sizes. Contrib Mineral Petrol 165:129-153

710 Mamani M, Wörner G, Sempere T (2010) Geochemical variation in igneous rocks of the Central
711 Andean orocline (13 °S to 18 °S): tracing crustal thickening and magmas generation
712 through time and space. Geological Society of America Bulletin 97:241–254

713 Mariño J, Samaniego P, Manrique N, Valderrama P, Macedo L (2019) Geología y mapa del
714 Complejo Volcánico Tutupaca. INGEMMET, Boletín, Serie C: Geodinámica e Ingeniería
715 Geológica, 66, 165 p., 2 mapas.

716 Médard E, Le Pennec JL, Francomme JE, Temel A, Nauret F (2013) Reconstructing the magma
717 feeding system of the Cappadocian ignimbrites (Turkey) through amphibole
718 thermobarometry. Goldschmidt conference, Florence, Italy

719 Médard E, Le Pennec JL (2019) Petrologic imaging of the magma chambers that feed super-
720 eruptions. Submitted

721 Morimoto N, Fabries J, Ferguson AK, Ginzburg IV, Ross M, Seifert FA, Zussman J (1988)
722 Nomenclature of pyroxenes. Am Mineral 73:1123-1133

723 Murphy MD, Sparks RSJ, Barclay J, Carroll MR, Brewer TS, Gene DE (2000) Remobilization
724 of Andesite Magma by Intrusion of Mafic Magma at the Soufriere Hills Volcano,
725 Montserrat, West Indies. J Petrol 41: 21–42

726 Mutch EJF, Blundy JD, Tattitch BC, Cooper FJ, Brooker RA (2016) An experimental study of
727 amphibole stability in low-pressure granitic magmas and a revised Al-in-hornblende
728 geobarometer. Contrib Mineral Petrol 171:85

729 Pallister JS, Hoblitt RP, Reyes AG (1992) A basalt trigger for the 1991 eruptions of Pinatubo
730 volcano? Nature 356:426-428

731 Peccerillo P, Taylor SR (1976) Geochemistry of Eocene calc-alkaline volcanic rocks from the
732 Kastamonu area, northern Turkey. Contrib Mineral Petrol 58:63–81

733 Poli S, Schmidt MW (1992) A comment on Calcic amphibole equilibria and a new amphibole-
734 plagioclase thermometrer by JD Blundy and TJB Holland. Contrib Mineral Petrol 104:208-
735 224

736 Prouteau G, Scaillet B (2003) Experimental constraints on the origin of the 1991 Pinatubo dacite.
737 J Petrol 44:2203–2241

738 Ridolfi F, Renzulli A, Puerini M (2010) Stability and chemical equilibrium of amphibole in calc-
739 alkaline magmas: an overview, new thermobarometric formulations and application to

740 subduc- tion-related volcanoes. Contrib Mineral Petrol 160:45–66

741 Ridolfi F, Renzulli A (2012) Calcic amphiboles in calc-alkaline and alkaline magmas:
742 thermobarometric and chemometric empirical equations valid up to 1130oC and 2.2 GPa.
743 Contrib Mineral Petrol 163:877–895

744 Rivera M, Thouret JC, Samaniego P, Le Pennec JL (2014) The 2006–2009 activity of Ubinas
745 volcano (Peru): petrology of the 2006 eruptive products and insights into genesis of andesite
746 magmas, magma recharge and plumbing system. J Volcanol Geotherm Res 270:122–141

747 Rivera M, Martin H, Le Pennec JL, Thouret JC, Gourgaud A, Gerbe MC (2017) Petro-
748 geochemical constraints on the source and evolution of magmas at El Misti volcano (Peru).
749 Lithos 268-271:240-259

750 Rubin AE, Cooper KM, Till CB, Kent AJR, Costa F, Bose M, Gravley D, Deering C, Cole J
751 (2017) Rapid cooling and cold storage in a silicic magma reservoir recorded in individual
752 crystals. Science 356:1154-1156

753 Ruprecht P, Bachmann O (2010) Pre-eruptive reheating during magma mixing at Quizapu
754 volcano and the implications for the explosiveness of silicic arc volcanoes. Geology
755 38:919–922

756 Ruprecht P, Wörner G (2007) Variable regimes in magma systems documented in plagioclase
757 zoning patterns: El Misti stratovolcano and Andahua monogenetic cones. J Volcanol
758 Geotherm Res 165:142–162

759 Ruprecht P, Bergantz G, Cooper K, Hildreth W (2012) The crustal magma storage system of
760 Volcán Quizapu, Chile, and the effects of magma mixing on magma diversity. Journal of

761 Petrology 53: 801- 840. doi:10.1093/petrology/egs002.

762 Rutherford MJ, Devine JD (1988) The May 18, 1980, Eruption of Mount St. Helens 3. Stability
763 and chemistry of amphibole in the magma chamber. J Geophys Res 93:11949-11959

764 Rutherford MJ, Hill P (1993) Magma ascent rates from amphibole breakdown: An experimental
765 study applied to the 1980–1986 Mount St. Helens eruptions. Journal of Geophysical
766 Research 981. 10.1029/93JB01613

767 Rutherford MJ, Devine JD (2003) Magmatic conditions and magma ascent as indicated by
768 hornblende phase equilibria and reactions in the 1995–2002 Soufrière Hills magma. J Petrol
769 44:1433–1454

770 Samaniego P, Le Pennec JL, Robin C, Hidalgo S (2011) Petrological analysis of the pre-eruptive
771 magmatic process prior to the 2006 explosive eruptions at Tungurahua volcano (Ecuador). J
772 Volcanol Geotherm Res 199:69-84

773 Samaniego P, Valderrama P, Mariño J, van Wyk de Vries B, Roche O, Manrique N, Chédeville
774 C, Liorzou C, Fidel L, Malnati J (2015) The historical (218 ± 14 aBP) explosive eruption of
775 Tutupaca volcano (Southern Peru). Bull Volcanol 77:51

776 Samaniego P, Rivera M, Mariño J, Guillou H, Liorzou C, Zerathe S, Delgado R, Valderrama P,
777 Scao V (2016) The eruptive chronology of the Ampato–Sabancaya volcanic complex
778 (Southern Peru). J Volcanol Geoth Res 323:110–128

779 Scaillet B, Evans BW (1999) The 15 June 1991 Eruption of Mount Pinatubo: I. Phase equilibria
780 and pre-eruption P–T–fO_2–fH_2O conditions of the dacite magma. J Petrol 40:381–411

781 Schiavi F, Bolfan-Casanova N, Withers AC, Médard E, Laumonier M, Laporte D, Flaherty T,

782 Gomez-Ulla A (2018) Water quantification in silicate glasses by Raman spectroscopy:
783 correcting for the effects of confocality, density and ferric iron. Chemical Geology 483:312-
784 331

785 Schmidt MW (1992) Amphibole composition in tonalite as a function of pressure: an
786 experimental calibration of the Al-in-hornblende barometer. Contrib Mineral Petrol
787 110:304-310

788 Shane P, Smith VC (2013) Using amphibole crystals to reconstruct magma storage temperatures
789 and pressures for the post-caldera collapse volcanism at Okataina volcano. Lithos 156-159:
790 159-170

791 Stix J, Torres R, Narváez L, Cortés G, Raigosa J, Gómez D, Castonguay R (1997) A model of
792 vulcanian eruptions at Galeras volcano, Colombia. J Volcanol Geotherm Res 77:285–303

793 Sun SS, McDonough WF (1989) Chemical and isotopic systematics of oceanic basalts:
794 implications for mantle composition and processes. In: Saunders AD, Norry MJ (eds)
795 Magmatism in the ocean basins. Special Publication 42, Geological Society, London, pp
796 313–345

797 Tepley FJ, de Silva S, Salas G (2013) Magma dynamics and petrological evolution leading to the
798 VEI 5 2000 BP eruption of El Misti volcano, Southern Peru. J. Petrol 54:2033-2065

799 Thouret J, Wörner G, Gunnell Y, Singer B, Zhang X, Souriot T (2007) Geochronologic and
800 stratigraphic constraints on canyon incision and Miocene uplift of the Central Andes in
801 Peru. Earth and Planetary Science Letters 263:151–166.

802 Valderrama P, Roche O, Samaniego P, van Wyk de Vries B, Bernard K, Mariño J (2016)

803 Dynamic implications of ridges on a debris avalanche deposit at Tutupaca volcano
804 (southern Peru). Bull Volcanol 78:14

805 Valdivia JG (1847) Fragmentos para la historia de Arequipa. Folletín de "El Deber", Arequipa,
806 109–111 p

807 Van Orman JA, Cherniak DJ, Kita NT (2014) Magnesium diffusion in plagioclase: Dependence
808 on composition, and implications for thermal resetting of the 26Al–26Mg early solar
809 system chronometer. Earth and Planetary Science Letters 385:79–88

810 Voight B, Komorowski JC, Norton GE, Belousov AB, Belousova M, Boudon G, Francis PW,
811 Franz W, Heinrich P, Sparks RSJ, Young SR (2002) The 1997 Boxing Day Sector Collapse
812 and Debris Avalanche, Soufriere Hills Volcano, Montserrat, W.I. In: Druitt T, Kokelaar BP
813 (eds), The eruption of Soufrière Hills Volcano, Montserrat, from 1995 to 1999. Mem Geol
814 Soc London 21:363– 407

815 Waters LE, Lange RA (2015) An updated calibration of the plagioclase-liquid hygrometer-
816 thermometer applicable to basalts through rhyolites. Am Mineral 100:2172–2184

817 Zamácola y Jaúregui JD (1804) Apuntes para la historia de Arequipa. Imp. De La Bolsa-
818 Guañamarca, N. 49. 1888

819 Zhang X, Liu B, Wang J, Zhang Z, Shi K, Wu S (2014) Adobe photoshop quantification (PSQ)
820 rather than point-counting: A rapid and precise method for quantifying rock textural data
821 and porosities. Computers and Geosciences 69:62–71

822

823 **Figure Captions**

824 **Fig. 1 a** Location of the Tutupaca Volcanic Complex (TVC) in the Peruvian volcanic arc. **b**
825 Geological map of the Eastern Tutupaca edifice (modified after Samaniego et al. 2015). RD –
826 Recent domes, P-PDC – Paipatja pyroclastic density currents deposits, DA – Debris avalanche
827 deposits, Z-PDC – Zuripujo pyroclastic density current deposits. Regional faults come from
828 Mariño et al. (2019)

829

830 **Fig. 2 a** View southwest of Tutupaca with the DA and P-PDC deposits (Photo by P.
831 Valderrama). Photos of the different eruptive products, **b** large dome block in the DA deposits,
832 note the person for scale, **c-d** breadcrust bombs in the P-PDC deposits

833

834 **Fig. 3 a** Microphotograph of a block in the debris avalanche deposit (TU-12-37) showing a large
835 plagioclase phenocryst (first group as described in text) and a small amphibole phenocryst (first
836 group) in a microlite-rich matrix. **b** Microphotograph of a recent dome sample (Dome V, TU-12-
837 70) showing a porphyritic texture with a partially vesiculated, microlite-rich matrix and
838 amphibole (amph), plagioclase (pl) and titanite (tnt) phenocrysts. Note the thin overgrowth rim
839 of the plagioclase crystal (second group described in text). **c-d** Amphibole phenenocrysts (Dome
840 I, TU-12-42 and Dome V, TU-12-70) of the first (c) and second (d) groups. **e** Clinopyroxene
841 phenocrysts in a P-PDC dacite sample (TU-12-77C). **f** Anhedral quartz (qtz) crystal in a P-PDC
842 dacite sample (TU-12-77C). **g** Mafic enclave hosted in a dacite (TU-14-01). **h** Silicic enclave
843 showing subhedral quartz, and inter-growing of amphibole and plagioclase into a crystallized
844 plagioclase-rich matrix (TU-14-08). All images are in polarized light

845

846 **Fig. 4** Major (**a-d**) and trace element concentrations (**e-j**) and ratios (**k-l**) for eruptive products of
847 the Recent (Eastern) Tutupaca, plotted versus SiO_2 as a differentiation index. Subdivision in K_2O
848 *vs.* SiO_2 diagram is from Peccerillo and Taylor (1976). B – basalt, BA – basaltic andesite, A –
849 andesite, D – dacite, MK – medium potassium, KH – high potassium. RD – Recent domes, P-
850 PDC – Paipatja pyroclastic density currents deposits, DA – Debris avalanche deposits, Z-PDC –
851 Zuripujo pyroclastic density currents deposits, ME – Mafic enclaves, SE – Silicic enclaves. Grey
852 fields represent data from Western and Basal Tutupaca (65 unpublished data, Mariño et al.
853 2019), with individual data points plotted only in **a** for clarity; Western and Basal Tutucapa (dark
854 and light grey diamonds, respectively)

855

856 **Fig. 5 a** Plagioclase phenocryst with an overgrowth rim corresponding to the second group
857 (dome VII, sample TU-12-14). **b** Rim-core-rim profile showing an increase in Anorthite and
858 FeO* in the overgrowth rim. **c** Plagioclase phenocryst with oscillatory zoning correspond to the
859 first group (P-PDC, TU-12-06A). **d** Core-rim profile showing a decrease Anorthite and FeO* in
860 the rim. **e** Amphibole phenocryst with an overgrowth rim, corresponding to the second group
861 (dome I, sample TU-12-42). **f** Profile of the amphibole showing an increase in ^{IV}Al and Mg#
862 towards the rim. **g** Zoned amphibole (dome I, sample TU-12-42). h Profile of the amphibole
863 showing a decrease in ^{IV}Al and an increase Mg# towards the rim. White dots in **a**, **c**, **e** and **g**
864 correspond to analysis points

865

866 **Fig. 6** Rare earth element diagrams normalized to chondrites (Sun and McDonough 1989) for
867 selected minerals. **a** High-Al amphibole, **b** Low-Al amphibole **c** plagioclase, **d** clinopyroxene **e**
868 titanite

869

870 **Fig. 7 a** K_2O (wt.%), **b** CaO (wt.%), **c** Al_2O_3 (wt.%) and **d** MgO (wt.%) compositions plotted
871 against SiO_2 (wt.%) for interstitial matrix glasses (MG) and melt inclusions (MI). Subdivision in
872 K_2O vs. SiO_2 diagram is from Peccerillo and Taylor (1976). Same symbols and fields as in Fig.
873 4. Note that MG and MI data roughly fall in the high-silica extension of the whole-rock Tutupaca
874 magmatic series

875

876 **Fig. 8 a** Na+K *vs.* ^{IV}Al, **b** ^{VI}Al *vs.* ^{IV}Al, and **c** Mg# *vs.* Si diagrams for Tutupaca amphiboles (after
877 Poli and Schmidt 1992). C – Core, R – Rim, M – Microlite, a.p.f.u. – atoms per formula unit. **d**
878 Amphibole microlite with an overgrowth rim, corresponding to the second group (sample TU-
879 12-70). TR, tremolite; ED, edenite; PG, pargasite; TS, tschermakite; HB, hornblende. Vectors
880 represent the exchange reactions discussed in the text

881

882 **Fig. 9 a** Temperature (°C) *vs.* ^{IV}Al for the two amphibole groups. **b** Temperature (°C) *vs.* Mg#.
883 Symbols correspond to rim analyses. Note that rims exhibit a coupled increase of ^{IV}Al and Mg#
884 with temperature

885

886 **Fig. 10** Diagram of **a** FeO* (wt.%) and **b** MgO (wt.%) against An (mol.%) for plagioclase. Same
887 symbols as Fig. 8. Fields for Soufrière Hills (Humphreys et al. 2009) and Misti-Andahua
888 volcanoes (Ruprecht and Wörner 2007, Tepley et al. 2013) for comparison. We observe a rough
889 positive trend in FeO* *vs.* An, whereas some scattering is observed in MgO *vs.* An. Note that
890 Tutupaca plagioclases display a limited chemical variation as compared with other well-studied
891 volcanic systems plotted here

892

893 **Fig. 11** Schematic conceptualization of the magmatic plumbing system below Tutupaca **a,** before
894 and, **b,** after hot and/or mafic magma recharge into the base of the dacitic reservoir. Magma
895 recharge triggers a thermal or "self-mixing" process that results in heating-induced convection of
896 the magma reservoir without physical mixing between the mafic magma and the pre-existing
897 dacitic magma. "Self-mixing" is the repercussion on the silicic magma of the close and sudden
898 contact with hotter and more mafic magma. The orange colour of the reservoir represents the
899 magma before recharge; the red colour the recharged magma, and the brown colour represents
900 the magma after the recharge event

901

902 **Supplementary material 1.** Description of the analytical methods

903 **Supplementary Material 2.** Trace elements composition in selected minerals from Tutupaca
904 dacites. PL – plagioclase, AMPH – amphibole, TTN – titanite, CPX – clinopyroxene. C – core, I
905 – interior, R – rim

906

907 **Supplementary Material 3. a** XAn and minor elements profiles through the sharp interface
908 between the outermost An-rich zone and the next An-poor inner zone of a plagioclase phenocryst
909 in a pumice from the P-PDC deposit. The ~10 μm outer zone records the last magmatic event
910 that affected the Tutupaca system, but more complex zoning is also present in the inner parts of
911 the crystal (see Fig. 5). **b** Magnification of the MgO profile (Profile 1), together with another
912 MgO profile taken in the same crystal. Diffusion modelling suggests a timescale of less than 10
913 years. Error bars are 2 sigma analytical errors from the electron microprobe

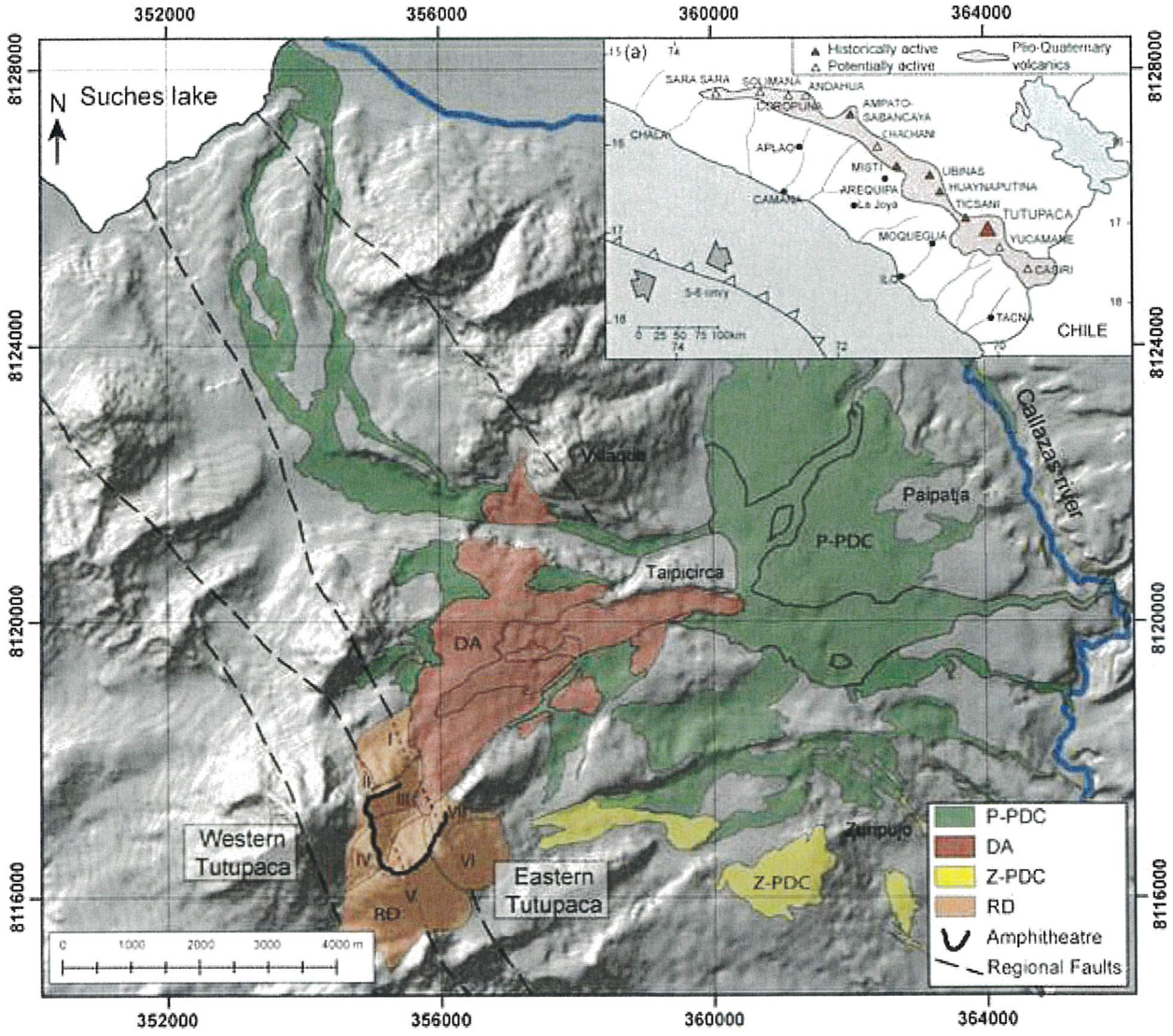
352000
356000
360000
364000
8128000
8124000
8120000
8116000
N
Suches lake
(a)
Historically active
Potentially active
Plio-Quaternary volcanics
SARA SARA
SOLIMANA
ANDAHUA
CHOPUNA
AMPATO-SABANCAYA
CHACHANI
CHACHI
APLAO
MISTI
UBINAS
AREQUIPA
HUAYNAPUTINA
CAMANA
La Joya
TICSANI
TUTUPACA
MOQUEGUA
YUCAMANE
CAGIRI
ILO
TACNA
CHILE
Nazca plate
0 25 50 75 100km
Callazas river
Yucamane
Paipata
P-PDC
Taipicirca
DA
I
II
III
IV
V
VI
VII
RD
Western Tutupaca
Eastern Tutupaca
Zumpujo
Z-PDC
0 1000 2000 3000 4000 m
P-PDC
DA
Z-PDC
RD
Amphitheatre
Regional Faults


a
Eastern
Tutupaca
Western
Tutupaca
Basal
Tutupaca
DA
P-PDC

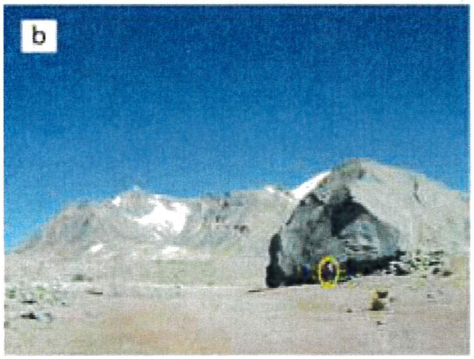
b


c


d

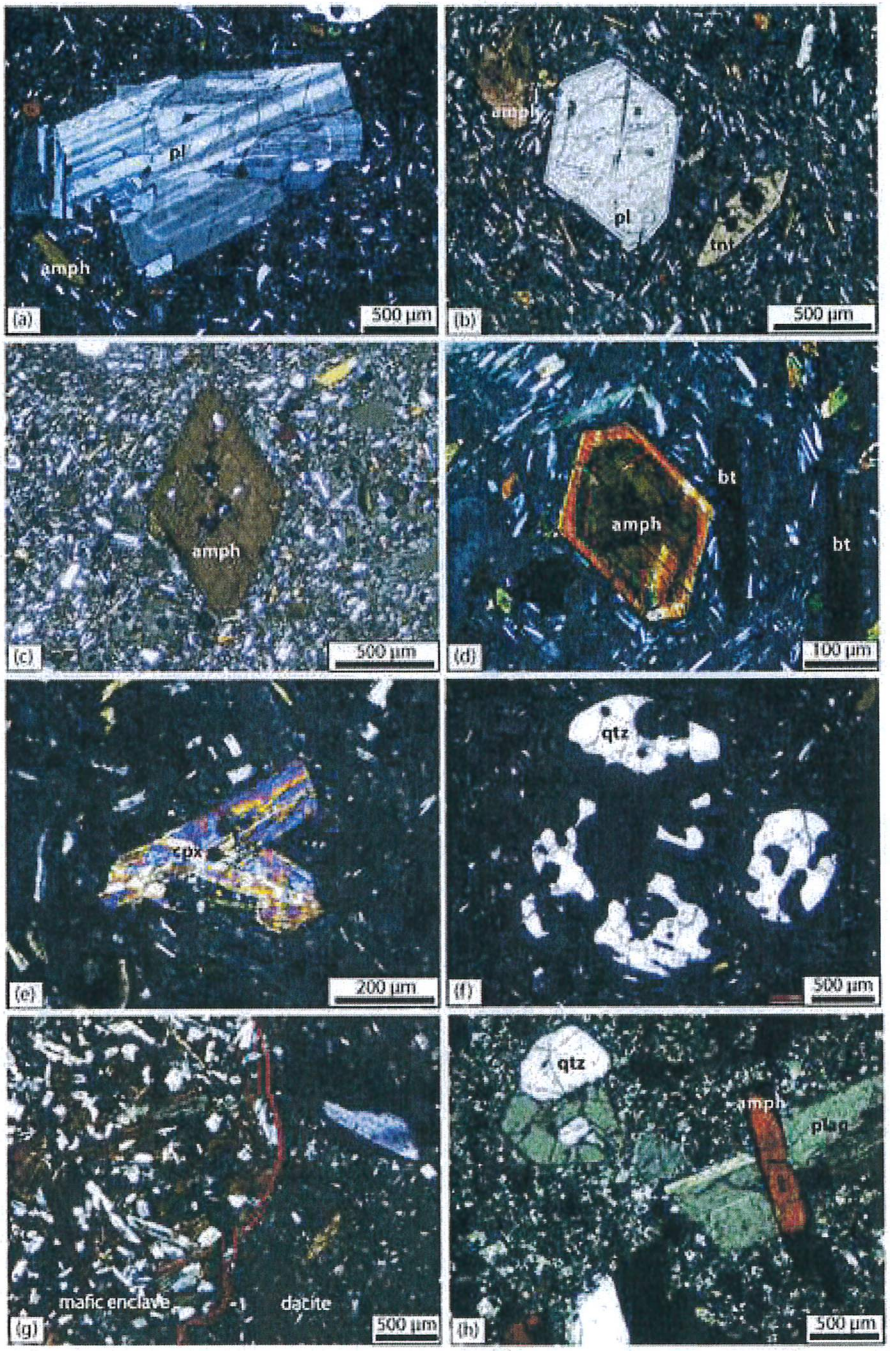
pl
amph
500 µm
(a)
amph
pl
500 µm
(b)
amph
500 µm
(c)
bt
amph
bt
100 µm
(d)
cpx
200 µm
(e)
qtz
500 µm
(f)
mafic enclave
dacite
500 µm
(g)
qtz
amph
plag
500 µm
(h)

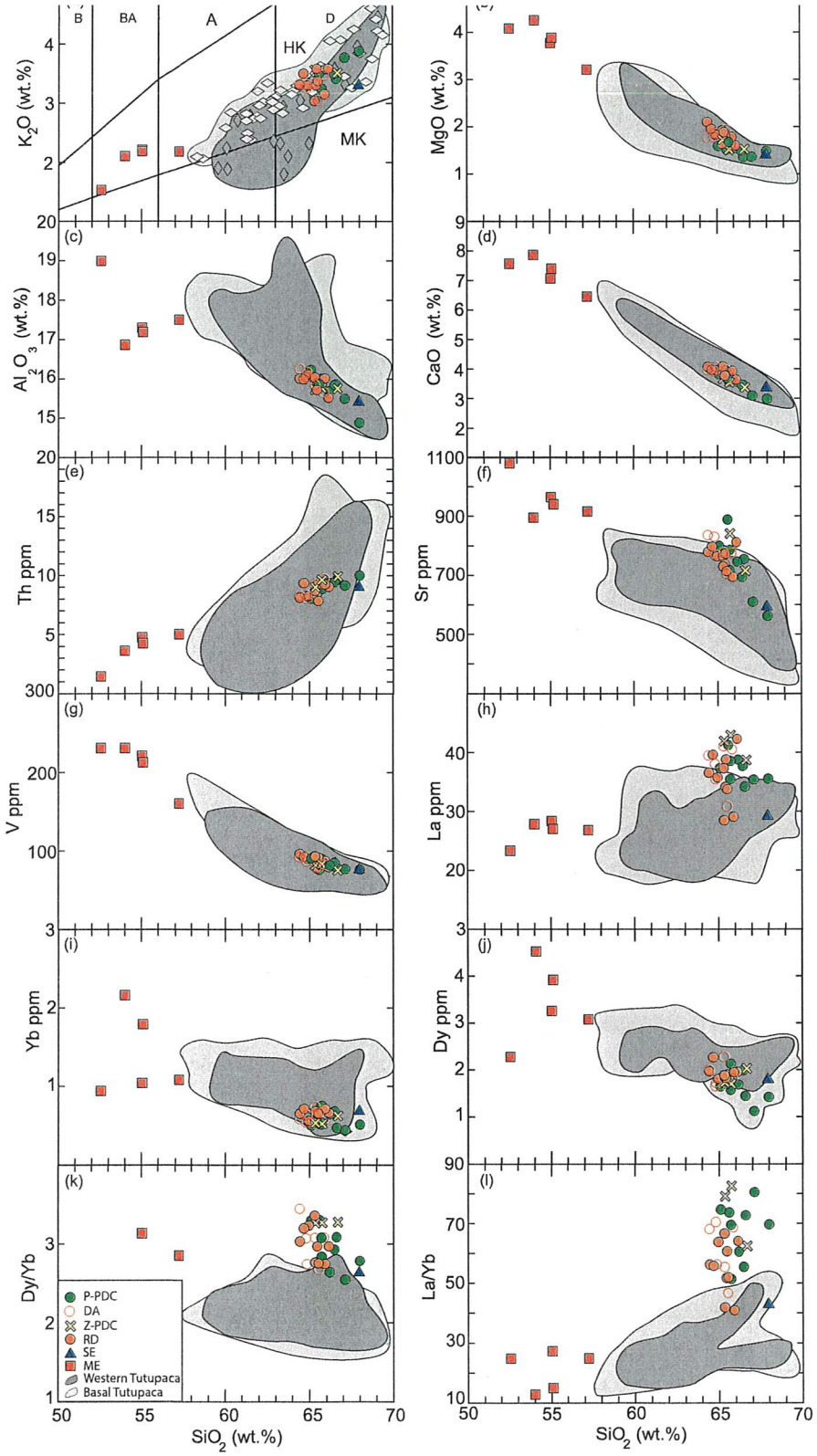
B
BA
A
D
HK
MK
K_2O (wt.%)
(b)
MgO (wt.%)
(c)
Al_2O_3 (wt.%)
(d)
CaO (wt.%)
(e)
Th ppm
(f)
Sr ppm
(g)
V ppm
(h)
La ppm
(i)
Yb ppm
(j)
Dy ppm
(k)
Dy/Yb
(l)
La/Yb
P-PDC
DA
Z-PDC
RD
SE
ME
Western Tutupaca
Basal Tutupaca
SiO_2 (wt.%)
SiO_2 (wt.%)

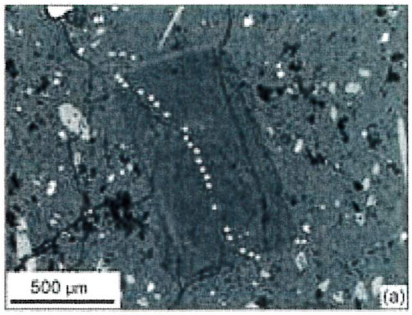
500 µm
(a)

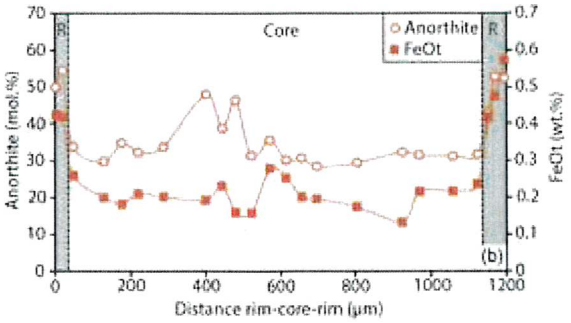
Core
Anorthite
FeOt
Anorthite (mol.%)
FeOt (wt.%)
Distance rim-core-rim (µm)
(b)

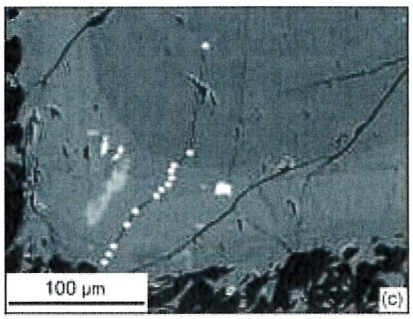
100 µm
(c)

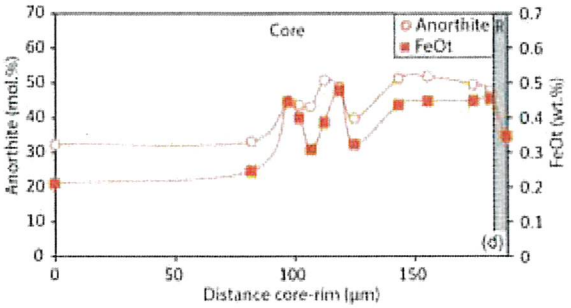
Core
Anorthite
FeOt
Anorthite (mol.%)
FeOt (wt.%)
Distance core-rim (µm)
(d)

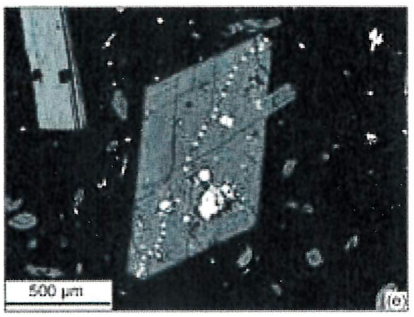
500 µm
(e)

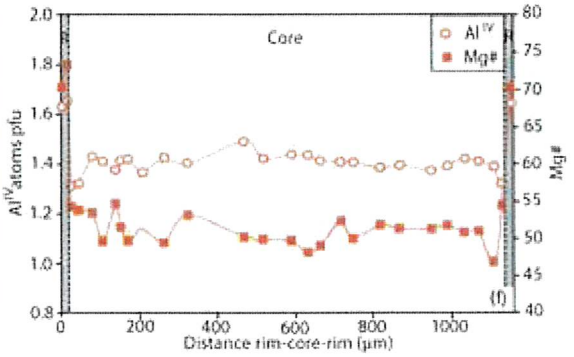
Core
Al IV
Mg#
AlIV atoms pfu
Distance rim-core-rim (µm)
(f)

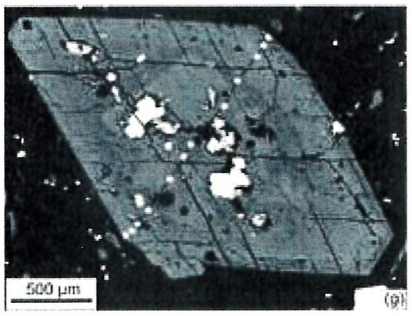
500 µm
(g)

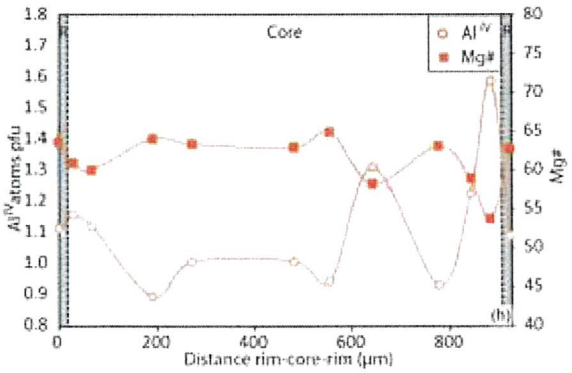
Core
Al IV
Mg#
AlIV atoms pfu
Distance rim-core-rim (µm)
(h)

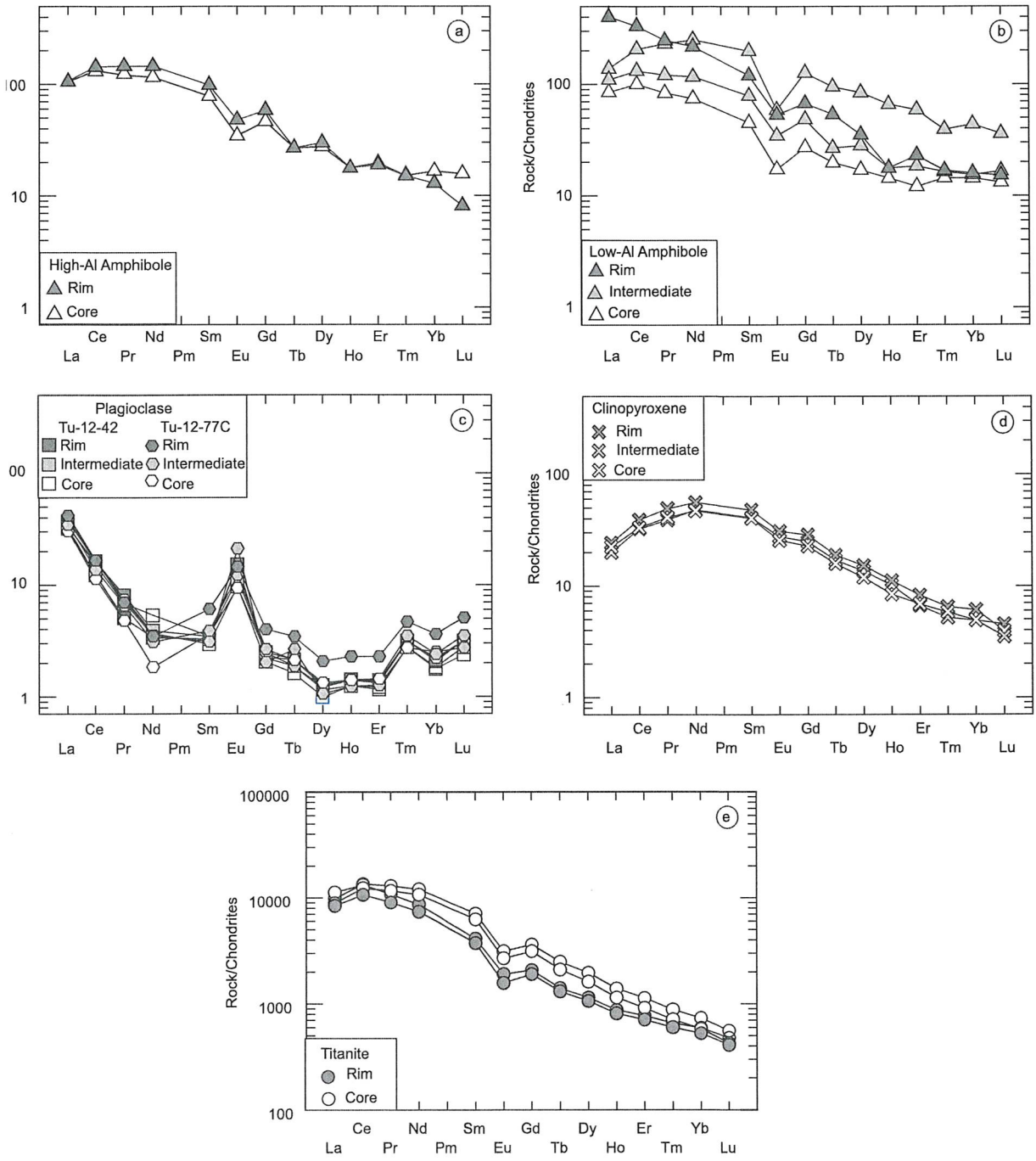
a
High-Al Amphibole
Rim
Core
b
Rock/Chondrites
Low-Al Amphibole
Rim
Intermediate
Core
c
Plagioclase
Tu-12-42
Tu-12-77C
Rim
Intermediate
Core
d
Clinopyroxene
Rim
Intermediate
Core
e
Titanite
Rim
Core
100000
10000
1000
100
10
1
La Ce Pr Nd Pm Sm Eu Gd Tb Dy Ho Er Tm Yb Lu

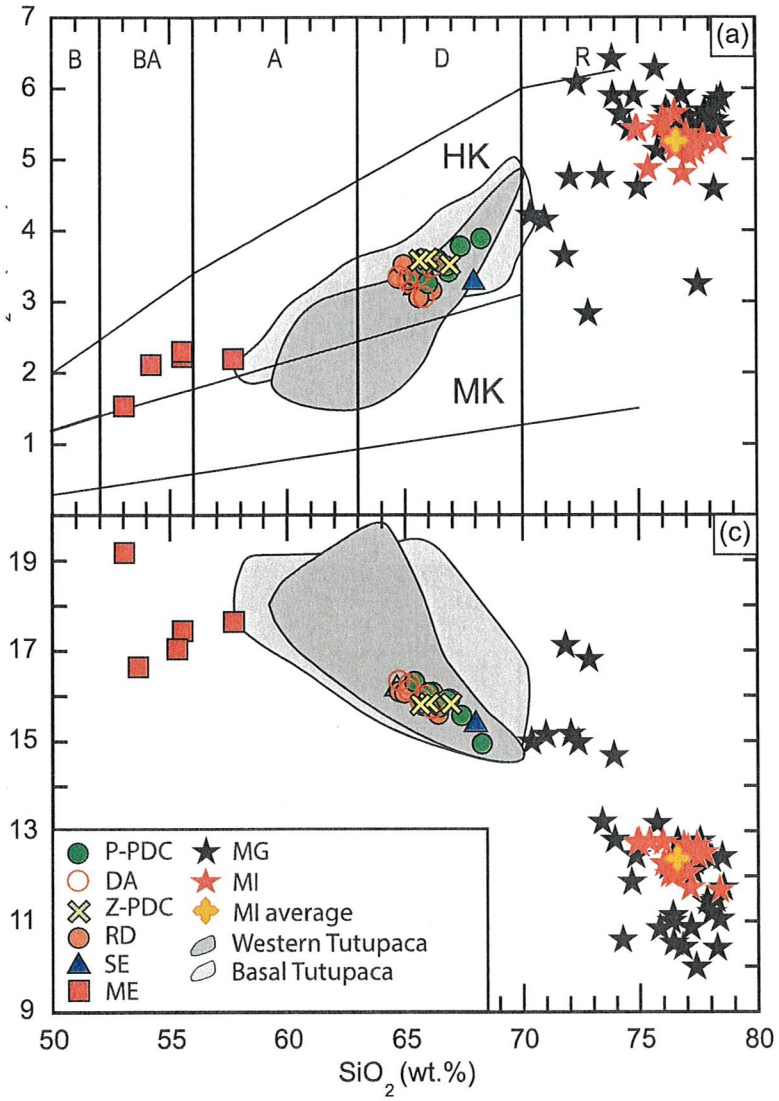
(a)
B
BA
A
D
R
HK
MK
(c)
P-PDC
DA
Z-PDC
RD
SE
ME
MG
MI
MI average
Western Tutupaca
Basal Tutupaca
SiO2 (wt.%)

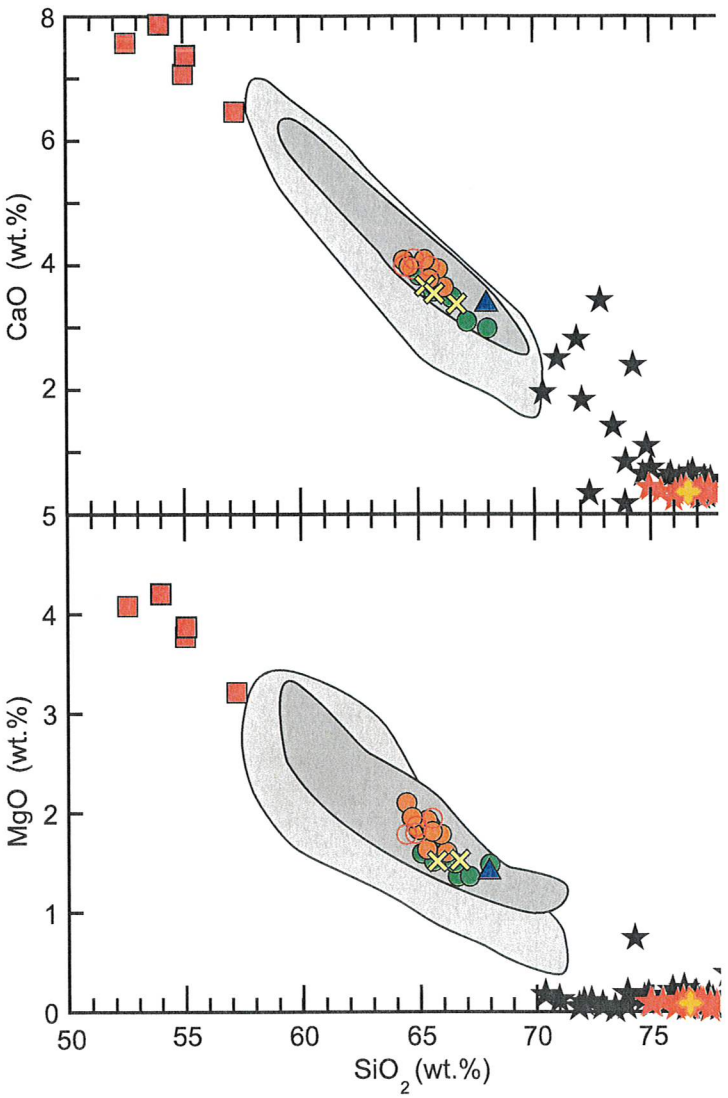
CaO (wt.%)
MgO (wt.%)
SiO2 (wt.%)

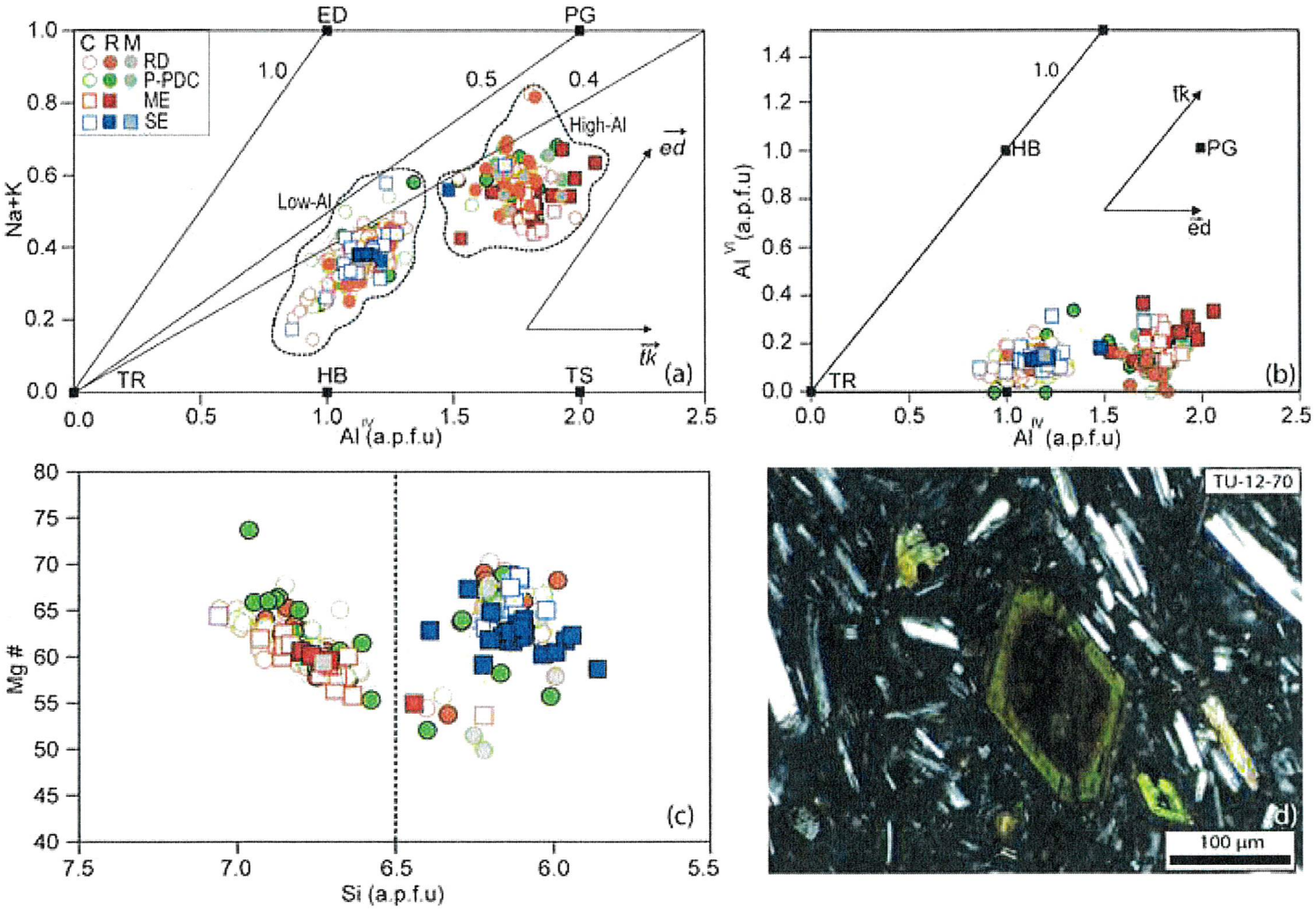
C R M
RD
P-PDC
ME
SE
ED
PG
1.0
0.5
0.4
High-Al
Low-Al
TR
HB
TS
(a)
Na+K
Al IV (a.p.f.u)
(b)
Al VI (a.p.f.u)
(c)
Mg #
Si (a.p.f.u)
TU-12-70
100 µm
(d)

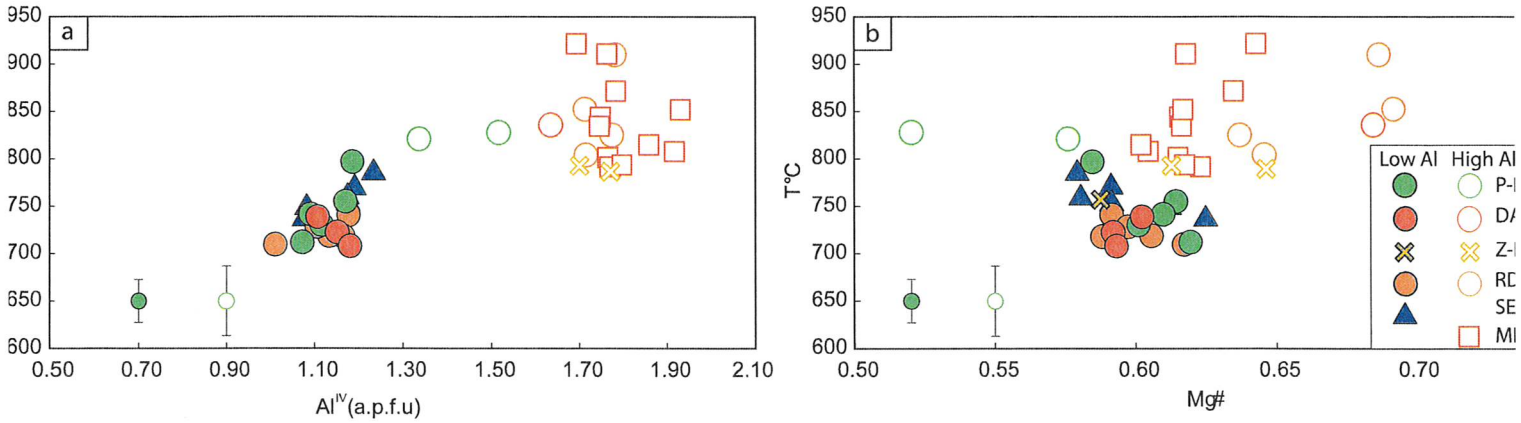
a
950
900
850
800
750
700
650
600
0.50
0.70
0.90
1.10
1.30
1.50
1.70
1.90
2.10
Al^IV(a.p.f.u)
b
T°C
0.50
0.55
0.60
0.65
0.70
Mg#
Low Al
High Al
P-I
DA
Z-I
RD
SE
MI

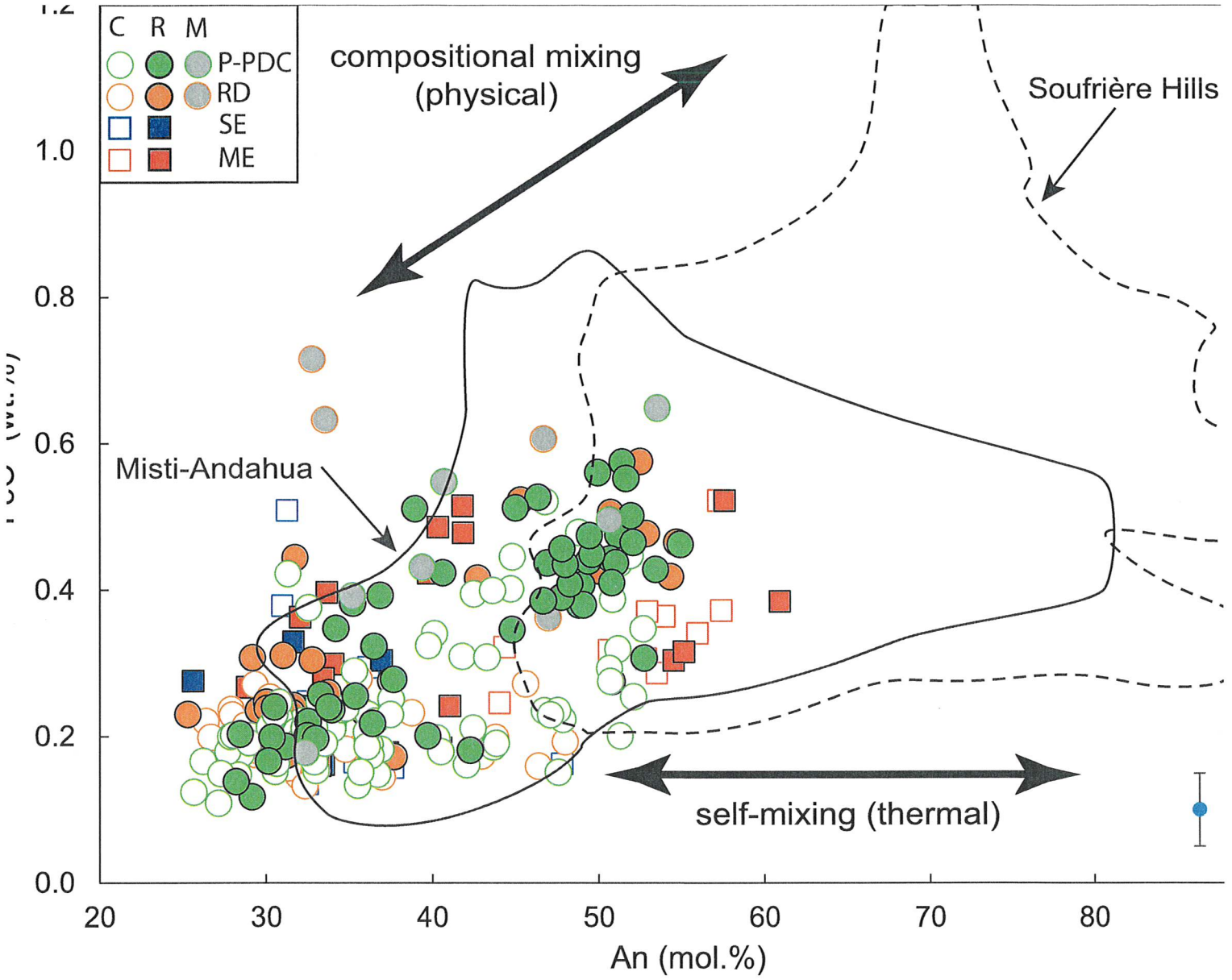
C R M
P-PDC
RD
SE
ME
compositional mixing
(physical)
Soufrière Hills
Misti-Andahua
self-mixing (thermal)
1.0
0.8
0.6
0.4
0.2
0.0
20
30
40
50
60
70
80
An (mol.%)

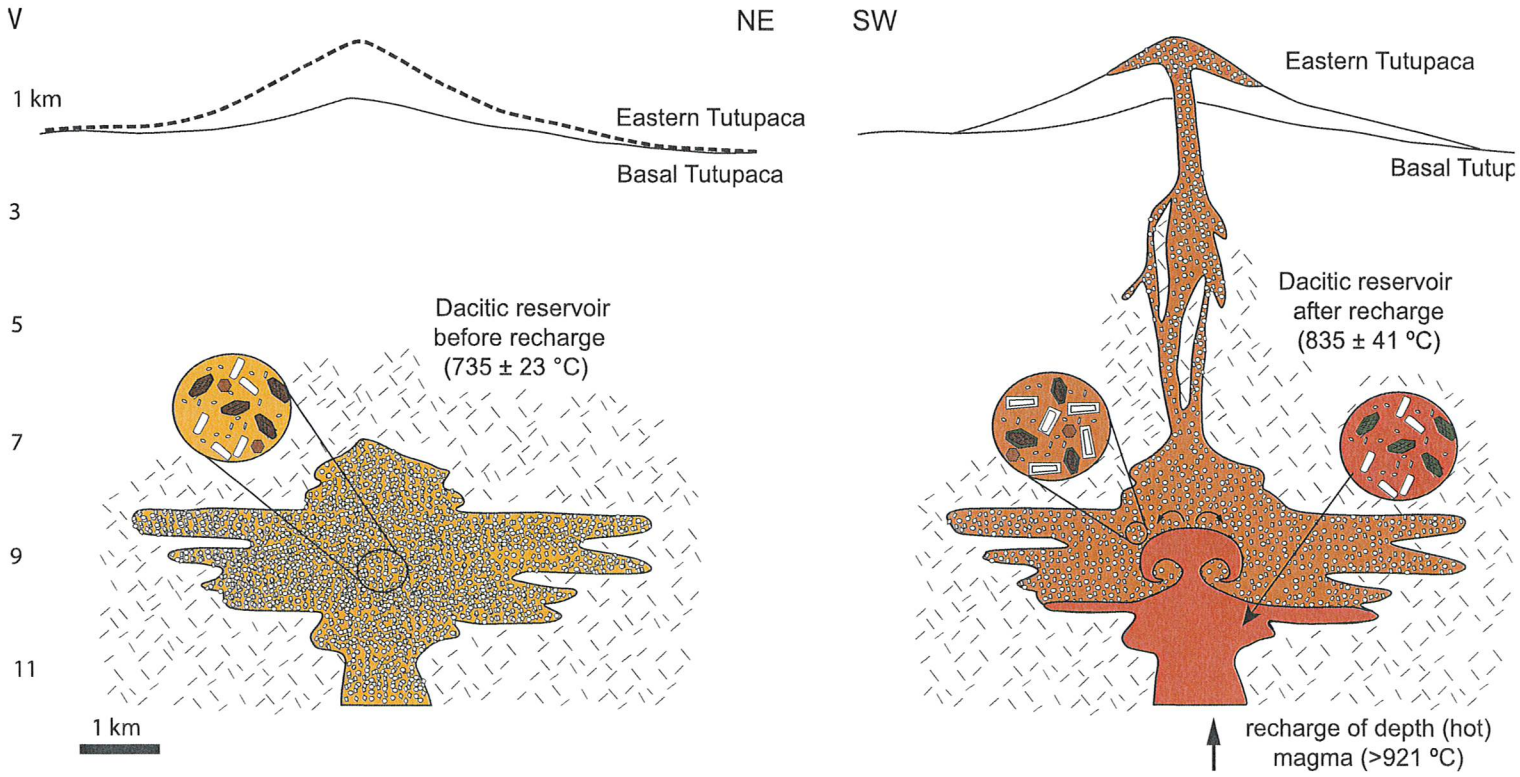
V
NE
SW
1 km
Eastern Tutupaca
Basal Tutupaca
3
5
7
9
11
Dacitic reservoir
before recharge
(735 ± 23 °C)
1 km
Eastern Tutupaca
Basal Tutup
Dacitic reservoir
after recharge
(835 ± 41 °C)
recharge of depth (hot)
magma (>921 °C)

Table 1 Whole-rock major (wt.%) and trace elements (ppm) analyses for Eastern Tutupaca samples *all iron as Fe_2O_3

Sample No.	TU-12-04B	TU-12-05	TU-12-37	TU-12-78	TU-12-09	TU-12-38	TU-12-06A	TU-12-06B	TU-12-06C	TU-12-22	TU-12-50	TU-12-66A	TU-12-69	TU-12-77A	TU-12-77C	TU-12-52	TU-12-68A	TU-12-76	TU-12-17	TU-13-22
Unit	DA	DA	DA	DA	DA	DA	P-PDC	P-PDC	P-PDC	P-PDC	P-PDC	P-PDC	P-PDC	P-PDC	P-PDC	Old DA	Old DA	Old DA	Old DA	Old DA
UTM North	8120200	8119960	8120709	8119412	8119422	8120301	8119537	8119537	8119537	8119036	8119458	8117932	8117789	8119045	8119045	8115103	8117375	8115272	8116326	8115279
UTM East	358990	357916	356952	357525	357418	356943	361158	361158	361158	362231	356938	359601	360112	362215	362215	353690	359411	356407	357225	354328
Altitude	4760	4846	4904	4858	4902	4916	4641	4641	4641	4595	4933	4814	4694	4680	4680	4960	4747	5218	5039	5099
SiO_2(wt.%)	63.4	64.2	64.3	66.3	64.4	64.4	64.6	65.3	64.1	64.4	66.3	64.3	64.6	65.9	66.9	64.0	63.5	63.9	64.5	66.1
TiO_2	0.8	0.8	0.7	0.8	0.8	0.7	0.7	0.7	0.7	0.6	0.7	0.8	0.7	0.7	0.7	0.8	0.9	0.8	0.7	0.8
Al_2O_3	16.0	15.9	16.0	16.1	15.3	15.6	15.6	15.6	16.0	14.9	14.5	15.6	15.3	16.0	15.9	15.3	15.7	15.3	15.6	15.8
Fe_2O_3*	4.4	4.4	4.3	4.4	4.2	4.2	4.3	3.9	4.4	3.9	3.9	4.1	4.1	4.3	4.1	4.3	4.4	4.4	4.0	4.3
MnO	0.1	0.1	0.1	0.1	0.1	0.1	0.1	0.1	0.1	0.1	0.1	0.1	0.1	0.1	0.1	0.1	0.1	0.1	0.1	0.1
MgO	1.8	1.8	1.8	1.9	1.6	1.9	1.6	1.3	1.6	1.3	1.4	1.5	1.5	1.6	1.5	1.7	1.9	1.9	1.4	1.8
CaO	3.9	3.9	4.0	3.9	3.6	3.9	3.5	3.4	3.8	3.0	2.9	3.6	3.5	3.8	3.5	3.7	3.9	3.8	3.5	3.8
Na_2O	4.5	4.5	4.3	4.3	4.2	4.2	4.2	4.3	4.3	4.0	3.7	4.3	4.1	4.3	4.2	4.2	4.2	4.1	4.4	4.1
K_2O	3.3	3.3	3.2	3.4	3.4	3.0	3.5	3.3	3.3	3.6	3.8	3.4	3.5	3.3	3.5	3.5	3.4	3.5	3.5	3.4
P_2O_5	0.3	0.3	0.3	0.3	0.3	0.2	0.3	0.2	0.3	0.2	0.3	0.4	0.3	0.3	0.3	0.3	0.3	0.3	0.3	0.3
LOI	0.2	0.2	0.3	0.3	0.5	0.7	1.0	0.1	0.2	2.5	1.6	0.1	0.7	0.8	1.0	0.4	0.2	0.4	0.0	0.3
Total	98.6	99.3	99.4	101.8	98.3	98.9	99.2	98.2	98.6	98.5	99.1	98.2	98.3	101.1	101.7	98.4	98.5	98.4	97.9	100.9
Sc (ppm)	6.7	6.7	7.3	7.0	5.8	7.6	5.4	4.7	5.5	4.1	5.8	4.7	5.6	6.8	5.9	6.7	6.7	7.2	4.6	6.2
V	92.6	91.8	87.1	86.0	82.7	79.0	88.3	78.8	90.5	77.0	76.5	76.0	81.7	89.7	85.0	85.1	83.7	88.9	78.5	84.1
Cr	12.8	11.9	10.7	12.8	9.4	12.3	10.9	9.4	11.7	8.0	7.7	8.4	11.0	12.0	9.8	11.7	10.6	11.6	8.9	8.6
Co	11.3	11.5	13.6	12.0	14.0	12.5	12.2	10.2	10.0	11.7	11.6	10.4	12.6	21.8	11.9	12.6	12.5	13.0	9.6	11.4
Ni	10.1	10.4	12.1	10.0	7.4	12.6	11.2	8.2	9.8	8.1	9.2	6.9	8.3	9.5	8.1	7.9	8.6	10.2	7.9	9.8
Rb	97.8	98.7	91.0	107.1	102.8	86.3	109.8	99.9	102.3	124.9	109.4	95.1	99.7	99.8	109.4	96.3	93.5	98.6	112.8	95.0
Sr	836.4	831.1	769.7	777.8	774.7	706.2	716.6	754.1	798.9	609.6	562.3	888.1	745.7	785.9	693.8	796.1	842.9	751.0	810.7	766.4
Y	9.1	8.5	8.5	10.5	8.8	9.4	7.4	6.7	7.9	6.6	7.3	7.7	8.6	10.3	9.6	9.3	9.6	9.2	8.0	10.5
Zr	148.8	142.2	129.6	151.5	134.7	82.5	134.4	90.9	134.3	143.9	151.7	144.9	145.9	141.9	144.8	150.5	148.1	142.6	129.9	148.8
Nb	8.5	7.8	7.6	8.8	9.0	8.4	6.8	7.3	8.3	6.2	7.9	9.4	8.9	8.9	8.0	8.6	9.0	8.4	8.1	8.8
Ba	1275.4	1374.6	1204.6	1341.5	1334.1	1113.9	1235.7	1295.9	1320.8	1302.4	1223.2	1297.7	1235.7	1230.9	1255.6	1262.0	1368.5	1292.2	1375.5	1323.0
La	39.5	38.1	35.5	41.1	40.6	30.9	35.5	34.2	37.3	35.4	35.5	41.3	38.8	38.5	37.7	39.8	41.6	38.9	41.8	41.8
Ce	78.7	74.6	72.4	78.9	79.5	62.9	67.3	65.9	70.0	66.4	67.8	79.1	76.3	74.3	71.9	79.6	79.6	78.2	80.3	79.7
Nd	31.8	30.2	28.1	33.5	32.0	25.5	26.3	24.8	28.7	25.5	26.0	30.8	31.0	31.2	29.5	32.8	33.4	31.3	32.9	33.2
Sm	6.0	4.8	4.6	5.8	5.2	4.5	4.2	3.8	5.0	4.3	3.7	4.7	5.1	5.1	5.0	4.9	5.3	5.4	5.7	5.5
Eu	1.3	1.2	1.3	1.4	1.3	1.2	1.2	1.2	1.3	1.1	1.1	1.4	1.3	1.3	1.2	1.4	1.5	1.4	1.4	1.4
Gd	3.5	3.3	3.4	4.1	3.6	3.2	3.1	2.7	3.0	2.9	2.7	3.2	3.2	4.0	3.5	3.5	3.7	3.7	3.3	3.9
Dy	2.0	1.7	1.7	2.3	1.8	1.8	1.6	1.4	1.6	1.1	1.4	1.8	1.7	2.1	2.0	1.9	1.9	1.8	1.6	2.2
Er	0.7	0.6	0.4	1.3	0.0	0.8	0.6	0.7	0.5	0.3	0.5	0.3	0.5	1.1	1.0	0.6	0.8	0.9	0.4	1.0
Yb	0.6	0.5	0.6	0.7	0.6	0.7	0.5	0.5	0.5	0.4	0.5	0.6	0.6	0.7	0.7	0.7	0.7	0.6	0.5	0.7
Th	8.3	8.3	8.0	9.3	9.7	9.4	9.1	9.6	8.0	9.2	10.0	8.7	9.4	8.8	9.4	9.3	8.7	8.9	9.3	9.4

Table 1 Continued

Sample No.	TU-12-80	TU-13-21A	TU-13-21B	TU-12-12	TU-12-27A	TU-12-79A	TU-12-14	TU-12-18	TU-12-42	TU-12-43	TU-12-70	TU-12-74	TU-13-08	TU-13-09	TU-13-19	TU-13-20	TU-14-01A	TU-14-01B	TU-14-01C	**TU-14-08**
Unit	Old-DA	Old-DA	Old-DA	Z-PDC	Z-PDC	Z-PDC	RD	RD	RD	RD	RD	RD	RD	RD	RD	RD	RD-enclave	RD-enclave	RD-enclave	RD-enclave
North	8115487	8115315	8115315	8117158	8118729	8116684	8117106	8116280	8117747	8117129	8115564	8115419	8117602	8117732	8116741	8116798	8117382	8117382	8117382	**8114880**
East	356817	354585	354585	357878	363116	363178	356850	356820	355675	355997	356205	355656	354814	355047	354679	354594	355852	355852	355852	**357155**
Altitude	5150	5140	5140	4882	4463	4460	5003	5071	5185	5417	5139	5298	5420	5417	5451	5468	5239	5239	5239	**5038**
SiO_2(wt.%)	64.9	67.0	66.3	64.7	64.3	66.6	63.7	64.4	64.5	64.5	63.5	65.3	64.5	64.8	64.7	64.2	55.3	53.0	57.9	**68.3**
TiO_2	0.8	0.7	0.8	0.8	0.8	0.7	0.7	0.7	0.8	0.7	0.8	0.8	0.6	0.6	0.7	0.8	1.5	1.0	1.0	**0.5**
Al_2O_3	15.6	15.2	15.2	15.5	15.5	15.7	15.8	15.8	15.5	15.5	15.8	15.3	15.7	15.9	15.6	15.9	17.4	19.1	17.7	**15.5**
Fe_2O_3*	4.5	4.0	4.0	4.1	4.3	3.9	4.3	4.3	4.2	4.4	4.6	4.1	4.0	4.3	4.4	4.5	9.0	9.3	8.1	**3.7**
MnO	0.1	0.1	0.1	0.1	0.1	0.1	0.1	0.1	0.1	0.1	0.1	0.1	0.1	0.1	0.1	0.1	0.1	0.1	0.1	**0.1**
MgO	1.8	1.4	1.5	1.5	1.7	1.5	1.8	1.6	1.8	1.9	2.1	1.6	1.7	1.9	1.8	1.9	3.8	4.1	3.2	**1.4**
CaO	3.5	3.2	3.3	3.5	3.6	3.4	3.9	3.8	3.7	3.9	4.0	3.6	3.9	4.0	3.7	3.9	7.1	7.6	6.5	**3.4**
Na_2O	4.1	4.0	4.0	4.4	4.3	4.2	4.3	4.3	4.2	4.2	4.2	4.2	4.1	4.3	4.2	4.2	3.6	4.6	4.0	**4.1**
K_2O	3.4	3.8	3.7	3.5	3.5	3.5	3.2	3.3	3.5	3.3	3.3	3.5	3.1	3.0	3.3	3.5	2.2	1.5	2.2	**3.3**
P_2O_5	0.3	0.3	0.3	0.3	0.3	0.3	0.3	0.3	0.3	0.3	0.3	0.3	0.2	0.2	0.3	0.3	0.5	0.3	0.3	**0.2**
LOI	1.4	1.3	0.8	0.0	0.4	0.6	0.2	0.0	0.4	0.3	0.3	0.2	1.6	1.0	0.3	0.3	0.3	0.2	0.0	**0.3**
Total	100.3	100.9	99.9	98.4	98.8	100.6	98.3	98.6	98.9	98.9	98.9	98.9	99.5	100.3	99.0	99.6	100.7	101.0	101.1	**100.9**
Sc (ppm)	6.1	4.8	4.9	5.0	6.2	5.4	6.5	5.6	7.3	7.6	7.8	6.2	6.9	7.5	6.8	7.0	13.4	18.4	13.1	**5.1**
V	87.8	80.0	75.4	83.5	82.0	75.3	91.0	93.2	78.1	89.4	96.5	79.3	87.4	93.0	91.6	92.8	220.8	230.8	160.4	**76.1**
Cr	12.7	8.2	7.6	9.7	9.4	10.3	11.7	11.6	9.3	11.8	12.6	9.3	13.5	14.0	10.5	11.2	10.9	23.8	1.3	**10.7**
Co	16.6	13.7	10.9	9.9	10.5	12.3	11.7	11.2	11.7	11.8	13.8	10.3	11.3	13.5	13.2	12.3	24.0	25.9	22.6	**9.5**
Ni	8.8	10.0	9.2	7.2	9.3	6.7	11.9	10.7	8.8	11.9	13.0	8.8	17.5	17.8	13.8	11.7	18.5	26.8	10.0	**7.9**
Rb	107.4	112.0	106.7	109.3	112.1	115.5	104.7	104.1	103.3	95.5	88.7	94.8	89.7	85.2	93.0	99.2	51.5	36.6	73.4	**77.5**
Sr	745.7	685.8	681.2	840.7	774.6	715.0	764.1	763.5	772.4	737.1	778.8	811.0	694.2	729.0	713.3	796.5	964.5	1080.0	915.9	**592.1**
Y	10.1	9.4	8.9	8.4	8.3	8.7	8.2	8.3	8.9	8.8	9.4	9.2	9.3	9.6	8.7	10.2	16.3	12.2	15.8	**9.4**
Zr	143.2	168.1	164.2	153.0	161.1	143.2	128.0	138.6	135.4	129.5	131.9	159.3	105.3	102.4	131.7	146.1	146.6	27.7	52.4	**24.5**
Nb	8.6	9.6	9.2	9.3	7.4	8.8	7.5	7.8	8.3	7.0	7.0	8.3	7.5	7.2	7.2	9.2	9.1	4.1	7.2	**6.9**
Ba	1337.9	1416.3	1390.1	1461.8	1357.4	1324.9	1289.4	1309.7	1321.0	1199.5	1247.3	1343.4	1129.3	1118.2	1281.1	1352.9	872.9	787.7	972.7	**1048.7**
La	41.1	42.0	40.5	42.9	41.9	38.7	35.7	37.3	38.8	34.2	36.6	42.3	29.1	28.5	33.8	39.6	28.4	23.4	26.8	**29.2**
Ce	79.4	79.2	75.5	81.2	82.8	94.2	69.2	70.6	75.7	67.3	72.0	82.8	57.9	56.0	66.3	76.2	59.2	46.0	50.9	**53.6**
Nd	34.2	31.9	30.8	32.8	33.0	30.2	27.8	28.6	31.0	27.5	30.3	34.4	23.7	23.0	27.3	33.6	32.7	21.9	26.5	**22.4**
Sm	6.1	5.3	5.0	5.7	5.6	5.2	4.7	5.5	5.3	4.7	5.3	5.9	3.8	4.2	4.7	5.5	7.2	4.3	5.7	**3.7**
Eu	1.5	1.3	1.1	1.3	1.4	1.2	1.1	1.1	1.3	1.3	1.3	1.5	1.1	1.1	1.1	1.5	1.8	1.1	1.5	**1.1**
Gd	4.3	3.8	3.5	3.6	3.6	3.6	3.2	3.1	3.5	3.2	3.4	3.6	3.4	3.5	3.6	4.3	5.1	3.7	4.4	**3.4**
Dy	2.2	2.1	1.8	1.7	1.7	2.0	1.8	1.9	1.9	1.8	2.0	2.0	2.0	1.9	1.8	2.3	3.3	2.3	3.1	**1.8**
Er	1.3	0.7	0.9	0.1	0.3	1.0	0.7	0.6	0.7	0.7	0.7	0.6	1.1	0.7	0.8	0.9	1.2	0.9	1.1	**1.2**
Yb	0.8	0.6	0.6	0.5	0.5	0.6	0.6	0.6	0.6	0.7	0.7	0.7	0.7	0.7	0.6	0.7	1.0	0.9	1.1	**0.7**
Th	9.3	10.4	10.0	9.6	9.0	9.9	8.3	8.4	9.2	8.3	8.1	9.1	9.2	8.7	7.8	9.4	4.8	1.4	5.0	**9.0**

Table 2 Selected plagioclase compositions (in wt.%) for samples of Tutupaca. PL: Plagioclase, C: Core, I: Interior, R: Rim. *all iron as FeO

Sample No.	TU-12-14				TU-12-22				TU-12-42				TU-12-77C				
Description	RD block				RD block				RD block				P-PDC bomb				
Analyse No.	PL1-C	PL1-R	PL2-C	PL2-R	PL1-C	PL1-R	PL2-C	PL2-R	PL2-C	PL2-R	PL4-C	PL4-R	PL1-C	PL1-R	PL2-C	PL2-I	PL2-R
SiO_2	60.8	54.2	61.2	54.9	61.7	60.1	55.2	56.0	59.8	59.7	61.6	61.7	61.8	57.5	56.8	61.6	56.8
TiO_2	0.0	0.0	0.0	0.0	0.0	0.0	0.0	0.0	0.0	0.0	0.0	0.0	0.0	0.0	0.0	0.0	0.1
Al_2O_3	24.4	28.2	23.6	26.8	23.7	24.4	27.7	27.5	25.0	24.5	23.8	23.9	24.0	25.8	27.5	24.1	25.6
FeO*	0.3	0.5	0.2	0.4	0.1	0.2	0.3	0.4	0.2	0.2	0.2	0.2	0.2	0.4	0.2	0.1	0.5
MnO	0.0	0.0	0.0	0.0	0.0	0.0	0.0	0.0	0.0	0.0	0.0	0.0	0.0	0.0	0.0	0.0	0.0
MgO	0.0	0.1	0.0	0.0	0.0	0.0	0.0	0.0	0.0	0.0	0.0	0.0	0.0	0.0	0.0	0.0	0.1
CaO	6.0	11.2	5.8	10.3	5.6	6.7	10.4	10.0	6.7	6.6	5.3	5.8	5.8	8.2	9.7	5.8	9.0
Na_2O	7.5	4.9	7.7	5.3	7.7	7.3	5.2	5.5	7.1	7.2	7.5	7.6	7.7	6.2	5.6	7.6	5.3
K_2O	0.9	0.3	0.9	0.4	0.9	0.7	0.4	0.4	0.6	0.7	1.0	0.8	0.8	0.6	0.4	0.8	0.7
Total	99.8	99.3	99.3	98.2	99.7	99.5	99.3	100.0	99.5	99.0	99.3	100.0	100.2	98.9	100.2	100.2	98.2
An (%)	29.0	55.0	27.9	50.5	27.1	32.5	51.2	48.8	32.8	32.2	26.4	28.1	28.0	40.6	47.8	28.3	46.4
Ab (%)	66.0	43.0	67.1	47.2	67.9	63.4	46.4	48.6	63.4	63.6	67.9	67.3	67.2	55.8	50.1	67.2	49.4

Table 2 Continued

Sample No.	TU-12-06A								TU-14-01A					TU-14-08			
Description	P-PDC bomb								Enclave in RD block					Siulicaous enclave in RD block			
Analyse No.	PL2-C	PL2-R	PL4-C	PL4-R	PL18-C	PL18-I	PL18-R	PL19-C	PL19-R	PL4-C	PL4-R	PL5-C	PL5-R	PL4-C	PL4-R	PL5-C	PL5-R
SiO_2	61.4	54.7	60.9	54.7	60.9	60.2	59.3	58.5	59.8	61.7	59.9	54.3	60.6	60.6	59.3	61.3	61.2
TiO_2	0.1	0.0	0.0	0.0	0.0	0.0	0.0	0.0	0.0	0.0	0.1	0.0	0.1	0.0	0.0	0.1	0.0
Al_2O_3	23.8	27.8	24.8	27.9	24.5	24.5	25.0	25.4	25.0	23.7	24.7	28.4	24.5	24.7	25.8	24.5	24.6
FeO*	0.2	0.5	0.2	0.5	0.2	0.2	0.4	0.4	0.4	0.1	0.2	0.4	0.4	0.2	0.2	0.2	0.2
MnO	0.0	0.0	0.0	0.0	0.0	0.0	0.0	0.0	0.0	0.0	0.0	0.0	0.0	0.0	0.0	0.0	0.0
MgO	0.0	0.1	0.0	0.0	0.0	0.0	0.0	0.0	0.0	0.0	0.0	0.0	0.0	0.0	0.0	0.0	0.0
CaO	5.7	10.6	6.7	11.1	6.3	6.7	7.6	8.0	7.2	5.6	6.7	11.0	6.5	6.5	7.7	6.1	6.4
Na_2O	7.7	5.1	6.1	4.7	7.4	7.0	6.6	6.2	6.6	7.7	7.0	5.0	7.1	7.3	6.9	7.3	7.5
K_2O	0.8	0.4	0.7	0.4	0.8	0.7	0.9	0.9	1.1	0.9	0.7	0.3	0.7	0.7	0.5	0.7	0.7
Total	99.5	99.3	99.4	99.4	100.0	99.3	99.8	99.5	100.2	99.7	99.2	99.5	99.8	100.1	100.3	100.2	100.7
An (%)	27.8	52.1	55.0	55.0	30.6	33.2	36.9	39.4	35.2	27.1	33.2	54.0	32.0	31.8	37.3	30.3	30.8
Ab (%)	67.6	45.5	42.5	42.5	64.9	62.6	57.9	55.3	58.3	67.9	62.7	44.5	63.9	63.9	59.8	65.5	65.3

Table 3 Selected amphibole compositions (in wt.%) for samples of Tutupaca. AMPH: Amphibole, C: Core, R: Rim. * all iron as FeO

Sample No.	TU-12-14				TU-12-42				TU-12-70				TU-12-06A			
Description	RD block				RD block				RD block				P-PDC bomb			
Analyse No.	AMPH1-C	AMPH1-R	AMPH2-C	AMPH2-R	AMPH1-C	AMPH1-R	AMPH2-MC	AMPH2-MR	AMPH1-C	AMPH1-R	AMPH3-MC	AMPH3-MR	AMPH1-C	AMPH1-R	AMPH4-C	AMPH4-R
SiO_2	46.0	46.3	47.2	45.5	46.9	46.3	46.6	42.9	46.3	47.8	42.6	42.5	41.9	40.6	47.1	43.4
TiO_2	1.2	1.3	1.5	1.4	1.3	1.3	1.4	3.3	1.4	1.1	3.2	3.3	3.2	3.0	1.2	2.9
Al_2O_3	7.6	7.3	6.9	7.7	7.0	7.3	7.2	10.5	7.7	6.7	10.5	10.8	12.0	12.0	7.0	10.1
FeO*	15.4	14.9	14.8	15.5	14.8	14.6	15.1	12.3	15.2	13.8	12.2	11.6	13.0	15.6	14.3	13.4
MnO	0.4	0.5	0.4	0.3	0.5	0.4	0.4	0.2	0.4	0.4	0.1	0.1	0.1	0.3	0.4	0.2
MgO	12.7	12.8	13.2	12.6	12.9	13.0	13.0	13.8	12.5	13.8	13.8	14.4	13.0	11.0	13.3	13.3
CaO	11.7	11.6	11.7	11.7	11.8	11.3	11.6	11.5	11.9	11.7	11.2	11.5	11.6	11.5	11.5	11.2
Na_2O	1.4	1.3	1.3	1.5	1.3	1.4	1.3	2.3	1.5	1.3	2.4	2.4	2.4	2.2	1.7	2.3
K_2O	0.8	0.8	0.7	0.9	0.7	0.8	0.8	0.9	0.8	0.7	0.9	0.8	0.9	1.0	0.7	0.9
Total	97.3	96.9	97.7	97.1	97.2	96.5	97.3	97.6	97.6	97.4	97.0	97.4	98.1	97.1	97.2	97.6
Mg#	59.5	60.4	61.3	59.1	60.9	61.3	60.6	66.6	59.5	64.1	66.8	68.9	64.1	55.7	62.4	63.9
^{IV}Al	1.2	1.2	1.1	1.2	1.1	1.1	1.1	1.7	1.2	1.0	1.7	1.8	1.9	1.9	1.1	1.6
^{VI}Al	0.1	0.1	0.1	0.1	0.1	0.1	0.1	0.1	0.2	0.2	0.1	0.1	0.2	0.2	0.1	0.1

Table 3 Continued

Sample No.	Tu-12-77C								TU-14-01				TU-14-08			
Description	P-PDC bomb								Enclave in RD block				Siliceous enclave in RD block			
Analyse No.	AMPH1-C	AMPH1-R	AMPH2-C	AMPH2-R	AMPH3-C	AMPH3-R	AMPH4-C	AMPH4-R	AMPH1-C	AMPH1-R	AMPH3-C	AMPH3-R	AMPH1-C	AMPH1-R	AMPH1-C	AMPH1-R
SiO_2	46.6	45.4	46.9	42.4	48.3	46.5	45.4	43.3	42.4	42.5	42.5	42.5	47.6	46.7	49.7	47.3
TiO_2	1.1	1.3	1.4	3.0	1.0	1.3	1.5	2.9	3.2	2.5	2.8	3.0	1.2	1.3	1.1	1.3
Al_2O_3	7.1	7.7	6.8	10.9	5.6	7.4	8.2	10.6	11.3	11.8	12.0	11.5	7.1	7.5	5.7	7.2
FeO*	15.1	15.7	15.1	13.6	14.0	14.6	15.7	12.5	11.6	13.9	13.8	11.8	14.9	15.2	14.0	15.1
MnO	0.5	0.4	0.4	0.2	0.5	0.3	0.4	0.2	0.1	0.3	0.2	0.2	0.5	0.4	0.5	0.5
MgO	12.8	12.3	13.0	13.0	14.3	12.8	12.4	13.6	14.2	12.7	12.7	13.7	13.3	12.8	14.2	13.0
CaO	11.3	11.5	11.3	11.1	11.5	11.3	11.2	11.1	11.0	11.1	11.2	11.3	11.8	11.8	11.6	11.4
Na_2O	1.3	1.6	1.3	2.3	1.1	1.3	1.5	2.1	2.3	2.1	2.2	2.2	1.3	1.3	1.1	1.4
K_2O	0.7	0.8	0.7	0.9	0.6	0.7	0.9	0.8	0.8	0.9	0.9	0.8	0.7	0.8	0.5	0.7
Total	96.7	96.7	96.8	97.3	96.9	96.4	97.2	97.2	96.9	97.8	98.3	97.1	98.4	97.8	98.4	97.9
Mg#	60.1	58.2	60.6	63.1	64.5	61.0	58.5	66.0	68.6	62.0	62.1	67.4	61.3	60.1	64.4	60.5
^{IV}Al	1.1	1.2	1.1	1.8	0.9	1.1	1.3	1.7	1.8	1.8	1.8	1.8	1.1	1.2	0.9	1.1
^{VI}Al	0.1	0.1	0.1	0.1	0.0	0.2	0.1	0.2	0.1	0.2	0.2	0.2	0.1	0.1	0.1	0.1

Table 4 Selected biotite compositions (in wt%) for samples of Tutupaca. BIO: Biotite, C: Core, R: Rim. *all iron as FeO

Sample No.	TU-12-14						TU-12-42		TU-12-70		TU-12-06A				TU-12-77C	
Description	RD block						RD block		RD block		P-PDC bomb				P-PDC bomb	
Analyse No.	BIO1-C	BIO1-R	BIO2-C	BIO2-R	BIO3-C	BIO3-R	BIO1-C	BIO1-R	BIO1-C	BIO1-R	BIO1-C	BIO1-R	BIO2-C	BIO2-R	BIO1-C	BIO1-R
SiO_2	36.5	36.5	36.5	36.1	36.4	36.1	36.7	36.6	36.8	36.7	37.2	37.4	36.7	38.3	36.7	37.0
TiO_2	4.5	4.5	4.4	4.5	4.1	4.2	4.2	4.3	4.6	4.6	4.2	4.5	4.2	4.5	4.3	4.2
Al_2O_3	13.5	13.3	13.2	13.3	13.5	13.4	13.3	13.5	13.5	13.2	13.4	13.7	13.5	14.3	13.4	13.1
FeO*	18.5	17.2	17.6	16.6	19.4	18.8	18.2	16.8	18.6	18.6	18.4	15.1	18.4	10.8	19.1	19.0
MnO	0.2	0.2	0.2	0.2	0.3	0.2	0.2	0.2	0.2	0.2	0.3	0.2	0.2	0.1	0.2	0.2
MgO	12.6	13.2	13.4	13.6	12.0	12.6	12.4	13.5	12.4	12.5	12.8	15.1	12.6	17.8	12.6	12.7
CaO	0.0	0.0	0.0	0.0	0.0	0.1	0.0	0.0	0.0	0.0	0.0	0.0	0.0	0.0	0.0	0.0
Na_2O	0.6	0.6	0.7	0.7	0.6	0.7	0.5	0.6	0.5	0.6	0.6	0.7	0.7	0.7	0.3	0.4
K_2O	9.1	9.0	9.0	8.8	9.1	9.2	9.1	9.2	9.4	9.3	9.8	9.3	9.3	9.3	9.1	9.5
Total	95.6	94.5	95.0	93.9	95.5	95.3	94.6	94.8	96.0	95.8	96.7	96.0	95.5	95.8	95.8	96.3

Table 5 Selected clinopyroxene, titanite and Fe-Ti oxydes compositions (in wt.%) for samples of Tutupaca. CPX: Clinopyroxene, TIT: Titanite, IL: Ilmenite, MAG: Magnetite, C: Core, R: Rim. *all iron as FeO

Sample No.	TU-12-42				Tu-12-06A				TU-12-06A		TU-12-42			
Description	RD block				P-PDC bomb				P-PDC bomb		RD block			
Analyse No.	CPX1-C	CPX1-R	CPX2-C	CPX2-R	CPX1-C	CPX1-R	CPX2-C	CPX2-R	TIT-C1	TIT-B1	TIT-C1	TIT-B1	TIT-C2	TIT-B2
SiO_2	52.6	51.0	53.4	53.2	51.5	52.9	50.9	52.1	29.7	30.1	29.5	29.5	29.8	30.1
TiO_2	0.5	0.9	0.3	0.5	0.7	0.6	0.7	0.6	38.0	37.3	37.4	37.4	36.6	37.8
Al_2O_3	1.8	3.2	0.5	0.7	3.2	2.3	3.3	2.5	0.8	1.2	1.1	1.1	1.3	1.1
FeO*	9.5	8.4	9.2	10.2	8.0	7.4	8.5	8.0	1.3	1.8	1.4	1.4	1.7	1.3
MnO	0.2	0.2	0.2	0.2	0.1	0.1	0.2	0.1	0.1	0.0	0.1	0.1	0.1	0.1
MgO	16.6	14.6	14.6	15.1	15.0	15.8	15.0	15.4	0.0	0.0	0.0	0.0	0.0	0.0
CaO	17.9	20.3	21.2	19.5	20.4	20.8	20.2	20.0	27.4	27.7	27.0	27.0	26.8	27.6
Na_2O	0.4	0.5	0.4	0.4	0.5	0.5	0.4	0.5	0.1	0.0	0.0	0.0	0.0	0.0
K_2O	0.0	0.0	0.0	0.0	0.0	0.1	0.0	0.1	0.0	0.0	0.0	0.0	0.0	0.0
Total	99.6	99.1	99.8	99.8	99.5	100.3	99.2	99.3	97.5	98.0	96.6	96.6	96.2	98.1
En (%)	47.6	43.0	41.8	43.3	44.0	45.2	43.8	44.9	-	-	-	-	-	-
Fs	15.4	13.8	14.8	16.4	13.2	11.9	13.9	13.2	-	-	-	-	-	-
Wo	37.0	43.1	43.4	40.3	42.8	42.9	42.3	41.9	-	-	-	-	-	-
Mg#	75.6	75.7	73.9	72.5	76.9	79.2	75.9	77.3	-	-	-	-	-	-

Table 5 Continued

Sample No.	TU-14-08				TU-12-77C		TU-12-14		TU-12-42		TU-14-01		
Description	Siliceous enclave in RD block				P-PDC bomb		RD block				Enclave in RD block		
Analyse No.	TTN-C1	TTN-B1	TTN-C2	TTN-B2	IL-C1	IL-B1	MAG-C2	MAG-B2	MAG-C1	MAG-B1	IL-C1	IL-C2	IL-B2
SiO_2	29.8	29.8	29.4	29.9	0.0	0.0	0.1	0.4	0.1	0.1	0.0	0.0	0.0
TiO_2	37.2	36.6	36.9	37.4	35.0	35.2	3.8	3.7	8.5	11.4	44.6	34.1	50.6
Al_2O_3	1.0	1.2	1.1	1.1	0.3	0.2	1.2	1.5	1.9	1.4	0.1	0.4	0.1
FeO*	1.4	1.9	1.5	1.5	58.2	59.3	87.2	84.9	79.9	79.1	52.4	57.5	45.6
MnO	0.1	0.1	0.1	0.1	0.5	0.6	0.4	0.4	0.6	0.7	0.7	0.5	0.6
MgO	0.0	0.0	0.0	0.0	2.2	1.0	0.9	0.8	1.9	1.7	1.8	1.2	1.2
CaO	27.1	27.3	26.6	27.4	0.1	0.3	0.0	0.1	0.0	0.1	0.0	0.0	0.0
Na_2O	0.1	0.0	0.0	0.0	0.0	0.0	0.0	0.1	0.0	0.0	0.0	0.0	0.1
K_2O	0.0	0.0	0.0	0.0	0.0	0.0	0.0	0.1	0.1	0.0	0.0	0.0	0.0
Total	96.7	97.0	95.5	97.5	96.3	96.6	93.6	91.9	93.0	94.5	99.7	93.7	98.2
Mg #	-	-	-	-	-	-	-	-	-	-	-	-	-

Table 6 Matrix glass and melt inclusions compositions (average ± standard deviation) for Tutupaca samples. *all iron as FeO

Sample No.	TU-12-42	TU-12-06A	TU-12-77C	TU-12-78	TU-14-01	TU-12-77C
Description	RD block	P-PDC bomb	P-PDC bomb	DA block	Enclave in RD block	MI in plagioclase
SiO_2	73.8 ± 2.8	75.3 ± 2.5	75.6 ± 2.1	75.4 ± 2.8	77.0 ± 1.6	76.4 ± 1.4
TiO_2	0.1 ± 0.1	0.3 ± 0.1	0.4 ± 0.1	0.3 ± 0.1	0.2 ±0.1	0.1 ± 0.06
Al_2O_3	15.1 ± 2.8	12.1 ± 1.7	11.7 ± 1.5	13.4 ± 1.5	12.6 ±0.9	12.3 ± 0.3
FeO*	1.0 ± 0.2	1.01 ± 0.2	0.9 ± 0.2	1.04 ± 0.3	1.1 ± 0.1	0.6 ± 0.2
MnO	0.05 ± 0.02	0.04 ± 0.04	0.1 ± 0.1	0.02 ± 0.03	0.03 ± 0.03	0.04 ± 0.04
MgO	0.1 ± 0.05	0.17 ± 0.19	0.1 ± 0.06	0.2 ± 0.2	0.1 ± 0.1	0.08 ± 0.02
CaO	1.7 ± 1.6	1.0 ± 0.8	0.7 ± 0.5	1.0 ± 0.8	0.5 ±0.1	0.4 ± 0.1
Na_2O	3.7 ± 1.2	3.1 ± 0.7	2.5 ± 0.8	3.1 ± 1.1	2.3 ± 1.0	3.4 ± 0.2
K_2O	4.9 ± 1.9	5.3 ± 0.5	5.3 ± 0.5	5.0 ± 1.0	5.4 ± 0.7	5.1 ± 0.22
Total	100.6	98.5	97.5	99.6	99.3	98.6 ± 1.1
H_2O (analysed by Raman spectrioscopy)						2.1 ± 0.3

Table 7 Pressure estimates based on Al-in-hornblende geobarometers. Barometers using total aluminium concentrations are temperature-dependent and should only be used for temperatures close to their calibration range. Barometers calibrated on rhyolitic and dacitic compositions cannot be used for the andesitic enclaves. Calculations that fit those quality criteria are reported in bold.

	Batometers calibrated for dacites to rhyolites					basalts to andesites
Reference	Schmidt (1992)	Mutch et al. (2016)	Johnson and Rutherford (1989)	Anderson and Smith (1995)	Médard and Le Pennec (2019)	Ridolfi and Renzulli (2012)
Calibration T	~ 669 °C	~ 733 °C	~ 760 °C	T corrected	T independent	~ 936 °C
Dacites, low Al (735 °C)	291 ± 47 MPa	**246 ± 27 MPa**	180 ± 42 MPa	**222 ± 44 MPa**	**230 ± 58 MPa**	97 ± 20 MPa
Dacites, high Al (835 °C)	561 ± 134 MPa	440 ± 105 MPa	420 ± 111 MPa	**210 ± 83 MPa**	**253 ± 55 MPa**	**218 ± 80 MPa**
Silicic enclave, low Al (735 °C)	305 ± 48 MPa	**254 ± 28 MPa**	193 ± 43 MPa	**227 ± 44 MPa**	**244 ± 18 MPa**	106 ± 19 MPa
Mafic enclave, high Al (840 °C)				292 ± 45 MPa	359 ± 40 MPa	**254 ± 59 MPa**